The Astrophysical Journal, 805:52 (18pp), 2015 May 20 doi:10.1088/0004-637X/805/1/52
© 2015. The American Astronomical Society. All rights reserved.

FUV VARIABILITY OF HD 189733. IS THE STAR ACCRETING MATERIAL FROM ITS HOT JUPITER?

I. Pillitteri[1], A. Maggio[1], G. Micela[1], S. Sciortino[1], S. J. Wolk[2], and T. Matsakos[3]
[1] INAF-Osservatorio Astronomico di Palermo, Piazza del Parlamento 1, I-90134, Palermo, Italy; pilli@astropa.inaf.it
[2] Harvard-Smithsonian Center for Astrophysics, Cambridge MA 02138, USA
[3] Department of Astronomy & Astrophysics, The University of Chicago, Chicago, IL 60637, USA
Received 2015 January 1; accepted 2015 March 18; published 2015 May 19

ABSTRACT

Hot Jupiters are subject to strong irradiation from their host stars and, as a consequence, they do evaporate. They can also interact with the parent stars by means of tides and magnetic fields. Both phenomena have strong implications for the evolution of these systems. Here we present time-resolved spectroscopy of HD 189733 observed with the Cosmic Origins Spectrograph on board *Hubble Space Telescope (HST)*. The star has been observed during five consecutive *HST* orbits, starting at a secondary transit of the planet ($\phi \sim 0.50-0.63$). Two main episodes of variability of ion lines of Si, C, N, and O are detected, with an increase of line fluxes. The Si IV lines show the highest degree of variability. The far-ultraviolet variability is a signature of enhanced activity in phase with the planet motion, occurring after the planet egress, as already observed three times in X-rays. With the support of MHD simulations, we propose the following interpretation: a stream of gas evaporating from the planet is actively and almost steadily accreting onto the stellar surface, impacting at 70°−90° ahead of the subplanetary point.

Key words: planet–star interactions – planetary systems – stars: activity – stars: chromospheres

1. INTRODUCTION

The significant fraction (∼10%) of known exoplanets with masses on the order of the Jupiter mass and orbiting within a few stellar radii (hot Jupiters) raises the question of their origin and evolution. Because of their proximity to the parent star, these planets are strongly irradiated, their upper atmospheres are bloated, and they do evaporate (Vidal-Madjar et al. 2003; Lecavelier des Etangs et al. 2004; Lecavelier Des Etangs et al. 2010; Linsky et al. 2010; Ben-Jaffel & Ballester 2013). It is plausible that the evaporating material forms a cometary tail and some sort of bow shock in front of the planet due to the interaction with the stellar wind (Cohen et al. 2011; Ben-Jaffel & Ballester 2013; Llama et al. 2013).

Furthermore, interactions of tidal and magnetic nature are likely to occur in systems with hot Jupiters (Cuntz et al. 2000; Saar et al. 2004; Cohen et al. 2009, 2010, 2011; Lanza 2009; Lanza et al. 2010, 2011). Stars can receive angular momentum from their hot Jupiters during the migration and circularization of the planet's orbit. The external input of angular momentum to the star reduces its decline with age during the main sequence due to wind losses. Because of the connection between stellar activity, age, and rotation, the stellar activity of the stars can be effectively boosted in the presence of hot Jupiters, mimicking a younger age, as demonstrated for the systems of HD 189733 and Corot-2 A (Pillitteri et al. 2010, 2011, 2014a; Schröter et al. 2011; Poppenhaeger & Wolk 2014). Tides can be produced on the stellar surface with a height proportional to d^{-3}, so the closer the planet, the stronger is the effect, which occurs twice per orbital period. However, in extreme cases, e.g., WASP-18 (Pillitteri et al. 2014b), the influence of the tidal perturbation could destroy the magnetic dynamo of stars with shallow convective zones. It is also suggested that the strong tidal stresses in WASP-18 reduce significantly the mixing inside the convective zone, as evidenced by a high Li abundance. This is at odds with the finding that planet host stars have depleted more Li than do single stars (Israelian et al. 2004; Bouvier 2008; Gonzalez 2008; Delgado Mena et al. 2014).

Magnetospheric interactions between planetary and stellar magnetic fields can be the source of additional reconnection events and perturbations of the magnetic field topology. As a result, more flares could manifest in systems with hot Jupiters than in single stars of the same age. Furthermore, the planetary magnetic field can efficiently trap the stellar wind and its angular momentum, modifying the losses of rotation and keeping the star rotating faster than expected for its age (Cohen et al. 2011).

Shkolnik et al. (2003, 2005, 2008) and Walker et al. (2008) reported evidence of chromospheric activity phased with the planetary orbital motion in the systems of μ and HD 179949 and HD 189733, probed by Ca II H & K lines. Interestingly, all cases exhibit a phase shift: the site of enhanced activity on the stellar surface is 70°−80° in the case of HD 179949 and 169° for μ and leading the subplanetary point.

In X-rays, we observed enhanced flare variability in HD 189733 after the eclipse of the planet ($\phi = 0.5$) in a restricted range of phases, $\phi = 0.52-0.65$ (Pillitteri et al. 2010, 2011, 2014a). The rate of such flare activity in HD 189733 is higher than in stars a few gigayears old and is similar to that of pre-main-sequence stars or stars more active than the Sun. Furthermore, this type of variability has not been observed at the planetary transits, raising the question whether HD 189733 has prevalent X-ray activity at some orbital phases of its hot Jupiter (Pillitteri et al. 2011, 2014a). An active spot on the stellar surface, at ∼70°−90° ahead of the subplanetary point, magnetically connected with the planet, and comoving with the planet had been hypothesized (Pillitteri et al. 2014a). Such a spot would emerge at the edge of the stellar disk when the planet is in a range of phases of $\phi = 0.52-0.65$, originating thus a phased variability.

Lanza et al. (2010) explains this phenomenon with an analytical model of the stellar field. The main hypothesis is that a magnetic link between the star and the planet exists if the

Table 1
Log of the *HST* Observations

Orbit	Nr.	Exposure Id.	Date	JD (days)	Planetary Phase*	Exposure (s)
I	1	lc0u01qjq	2013:09:12T10:14:21	2456547.92663194	0.4996	431.0
	2	lc0u01qlq	2013:09:12T10:23:27	2456547.93295139	0.5025	440.0
	3	lc0u01qnq	2013:09:12T10:32:42	2456547.93937500	0.5054	440.0
	4	lc0u01qpq	2013:09:12T10:41:57	2456547.94579861	0.5083	440.0
II	5	lc0u01qrq	2013:09:12T11:31:45	2456547.98038194	0.5239	640.2
	6	lc0u01qtq	2013:09:12T11:44:20	2456547.98912037	0.5278	652.2
	7	lc0u01qvq	2013:09:12T11:57:16	2456547.99810185	0.5318	654.2
	8	lc0u01qxq	2013:09:12T12:10:14	2456548.00710648	0.5359	649.2
III	9	lc0u01qzq	2013:09:12T13:07:25	2456548.04681713	0.5538	648.2
	10	lc0u01r1q	2013:09:12T13:20:17	2456548.05575231	0.5578	646.2
	11	lc0u01r3q	2013:09:12T13:33:70	2456548.06466435	0.5618	646.2
	12	lc0u01r5q	2013:09:12T13:45:57	2456548.07357639	0.5659	646.2
IV	13	lc0u01r7q	2013:09:12T14:43:70	2456548.11327546	0.5838	648.2
	14	lc0u01r9q	2013:09:12T14:55:59	2456548.12221065	0.5878	646.2
	15	lc0u01rbq	2013:09:12T15:08:49	2456548.13112269	0.5918	646.2
	16	lc0u01rdq	2013:09:12T15:21:39	2456548.14003472	0.5958	646.2
V	17	lc0u01rfq	2013:09:12T16:18:50	2456548.17974537	0.6137	648.2
	18	lc0u01rhq	2013:09:12T16:31:42	2456548.18868056	0.6177	646.2
	19	lc0u01rjq	2013:09:12T16:44:32	2456548.19759259	0.6218	646.2
	20	lc0u01rlq	2013:09:12T16:57:22	2456548.20650463	0.6258	646.2

Note. Orbits are labeled with I, II, III, IV, and V roman numbers. Four dithered exposures are obtained for each orbit, and thus a total of 20 exposures are obtained. Exposure times are of ∼640−650 s during all orbits but I, where exposures were 430−440 s. The ephemeris for calculating planetary phases is from Triaud et al. (2009).

planet is sufficiently close to the star, as in the case of hot Jupiters. The lines of the magnetic field of the star could connect with the dipolar field of the planet via a bent path and generate thus the phase lag. The relative motion of the planet with respect to the star is a key ingredient for generating such a configuration. In Lanza (2012) this model is further refined, with the planet motion inducing reconnection events near the surface of the star.

Cohen et al. (2011) modeled the magnetic SPI in HD 189733, including a more realistic stellar magnetic field. Their magneto-hydrodynamical (MHD) simulations show that at certain phases the planet can induce reconnection events and flares if the planet encounters a locally enhanced stellar magnetic field. The same model predicts the rate of exoplanet atmosphere loss and the cometary tail that the planet motion is winding around its orbit. Preusse et al. (2006) and Kopp et al. (2011) modeled the interaction between planet and star by means of Alfvènic waves hitting the surface of the star, generated by the planet acting as a conductor moving within the stellar magnetic field and the stellar wind. This model can reproduce well the observed phase lag of chromospheric activity that arises from the relative motion of the planet and the star.

Among the systems with hot Jupiters, HD 189733 is a privileged target where we can study star-planet interaction (SPI) effects, planet evaporation, and the dynamics of the planetary gas around the host star. It is composed of a K1.5 V-type star as a primary component ($P_{\rm rot}$ = 11.9 days, d = 19.3 pc from the Sun) and an M4 companion, HD 189733B, at 3200 AU from the primary. HD 189733 A hosts a hot Jupiter class planet (HD 189733b) at a distance of only 0.031 AU (about 8.5 stellar radii) with an orbital period of ∼2.22 days (Bouchyzz et al. 2005).

In this paper we present observations of HD 189733 obtained with the Cosmic Origins Spectrograph (COS) on board *Hubble Space Telescope (HST)*. The aim of our observations is to obtain time-resolved spectroscopy of HD 189733 at the postplanetary eclipse phases, as observed with *XMM-Newton*, in order to find signatures of SPI in the far ultraviolet (FUV) and to better recognize and understand any phased activity in HD 189733. Previous observations in the FUV of HD 189733 with *HST* COS and Space Telescope Imaging Spectrograph (STIS) have focused on the planetary transits. These observations revealed the evaporation of the planetary atmosphere and an estimate of the mass loss (Lecavelier Des Etangs et al. 2010) and an asymmetry of ingress and egress, implying a bow shock in front of the planet due to the interaction between the stellar wind and the planetary escaping atmosphere (Lecavelier des Etangs et al. 2012; Ben-Jaffel & Ballester 2013; Bourrier et al. 2013; Llama et al. 2013). Motivated by our findings in X-rays, we argue that observing HD 189733 at the planetary eclipse in the FUV can offer new insights on the dynamics of the gas evaporating from the planet and of the structure of the chromosphere and transition region of the star. The paper is structured as follows. In Section 2 we describe the observations and the data analysis, and Section 3 details the results. In Section 4 we discuss the results, and in Section 5 we present our conclusions.

2. OBSERVATIONS AND DATA ANALYSIS

We observed HD 189733 with the *HST* and COS spectrograph on 2013 September 12. The observations were carried along five consecutive *HST* orbits, spanning the planetary orbital phases of 0.4996 through 0.6258 (see Table 1 and Figure 1, left panel). We used the grating G130M with a central wavelength of 1309 Å that encompasses the range 1150–1450 Å and has a gap between the two detector segments in the range ∼1294−1309 Å. The effective area of COS paired with grating G130M is above 1500 $\rm cm^2$ with a peak of 2500 $\rm cm^2$ around 1220 Å. For the transit and period, we used

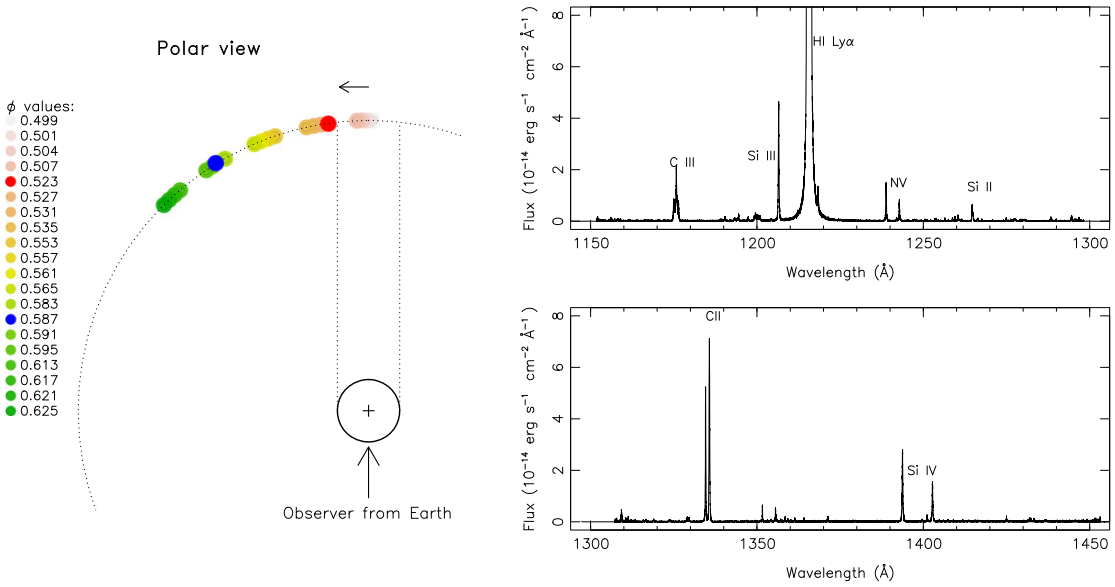


Figure 1. Left panel: schematic of the planetary phases during the COS exposures. Right panel: average spectrum obtained from the five *HST* orbits and the sum of the COS exposures. We marked the main ion lines in the two wavelength ranges. A detailed plot of the spectrum is available at www.astropa.inaf.it/~pilli/hd189733_hst_cos.pdf.

the ephemeris from Triaud et al. (2009), which is based on the analysis of optical spectra obtained with the High Accuracy Radial velocity Planet Searcher (HARPS) spectrograph at the ESO 3.6 m telescope in La Silla (Chile). When using the ephemeris from Agol et al. (2010), based on *Spitzer* observations, this would result in a systematic shift of ∼−249.1 s with respect to the optical ephemeris of Triaud et al. (2009).

The average spectrum from the five orbits is shown in Figure 1, right panel. The total exposure is about 12.1 ks. The main lines in this range are the H I Lyα, Si II, Si III, and Si IV lines, the C II and C III lines, and the N V lines. A list of these lines, with the peak of formation temperature, line intensity, and spectroscopic terms, is given in Table 2. These data are taken from the Chianti database (Dere et al. 1997; Landi et al. 2013). However, other small lines are visible in our spectra and missing from Chianti. To identify these lines, we used the National Institute of Standards and Technology (NIST) database (Kramida et al. 2014). To help with the identification of the lines, we produced an atlas of the spectrum[4], plotted in pieces of 10 . In each panel, the lines from Chianti are labeled, and tick marks at the NIST wavelengths of lines of different elements (only those with relative accuracy ⩽50%) are indicated with different colors. Most of these lines are from Fe ions, Al, Si, and S. Also, air-glow lines are marked with light-blue bands across the spectrum. Figure 2 shows a close-up plot of selected line profiles for three spectra: an average spectrum of the first orbit, and exposure numbers 5 and 14, which show two episodes of flux increases in several lines.

We label the orbits with I, II, III, IV, and V roman numbers. For each orbit we have available four dithered exposures as part of the ordinary strategy of data acquisition. The dithering along the dispersion axis reduces the effects of inhomogeneous sensitivity pixel by pixel. The typical exposure of the single exposures is about 640–650 s. Only during the first orbit were the exposures shorter, on the order of 430−440 s, because of the initial target acquisition overhead.

With the IRAF and CALCOS package we have transformed the calibrated tables and spectra into a format suitable to be read from other software (e.g., Python and R). Our analysis is aimed at a fine time-resolved spectroscopy by exploiting the capability of COS to acquire single photons with their arrival time. This feature allows us to further slice the exposures

Table 2
List of Prominent Lines in the Spectral Range 1150–1450 Å Used in Our COS Observations

Ion	Wavelength (Å)	log(T) (K)	Transition
C III	1174.93	4.80	$2s2p^3P_1 - 2p^2\ ^3P_2$
C III	1175.26	4.80	$2s2p^3P_0 - 2p^2\ ^3P_1$
C III	1175.59	4.80	$2s2p^3P_1 - 2p^2\ 3_1^P$
C III	1175.71	4.80	$2s2p^3P_2 - 2p^2\ 3_2^P$
C III	1175.99	4.80	$2s2p^3P_1 - 2p^2\ 3_0^P$
C III	1176.37	4.80	$2s2p^3P_2 - 2p^2\ 3_1^P$
S III	1200.96	4.70	$3s^23p^2\ 3_2^P - 3s3p^3\ 3_3^D$
Si III	1206.50	4.70	$3s^21_0^S - 3s3p^1P_1$
Si III	1206.56	4.80	$3s3p^1P_1 - 3s3\ d^1D_2$
H I	1215.67	4.50	$1s^2S_{1/2} - 2p^2P_{3/2}$
H I	1215.68	4.50	$1s^2S_{1/2} - 2p^2P_{1/2}$
O V	1218.34	5.30	$2s^2\ ^1S_0 - 2s^2p^3P_1$
N V	1238.82	5.20	$1s^2\ ^2s_2S_{1/2} - 1s^22p^2P3/2$
N V	1242.81	5.20	$1s^22s^2S_{1/2} - 1s^22p^2P_{1/2}$
Si II	1264.74	4.50	$3s^23p^2P_{3/2} - 3s^23\ d^2D_{5/2}$
C II	1334.54	4.50	$2s^22p^2P_{1/2} - 2s2p^2\ ^2D_{3/2}$
C II	1335.66	4.50	$2s^22p^2P_{3/2} - 2s2p^2\ ^2D_{3/2}$
C II	1335.71	4.50	$2s^22p^2P_{3/2} - 2s2p^2\ ^2D_{5/2}$
Si IV	1393.76	4.90	$3s^2S_{1/2} - 3p^2P_{3/2}$
O IV	1401.16	5.10	$2s^22p^2P_{3/2} - 2s2p^2\ ^4P_{3/2}$
Si IV	1402.77	4.90	$3s^2S_{1/2} - 3p^2P_{1/2}$

Note. Lines falling in the gap 1294–1309 Å are not listed.

[4] Available at www.astropa.inaf.it/~pilli/hd189733_hst_cos.pdf.

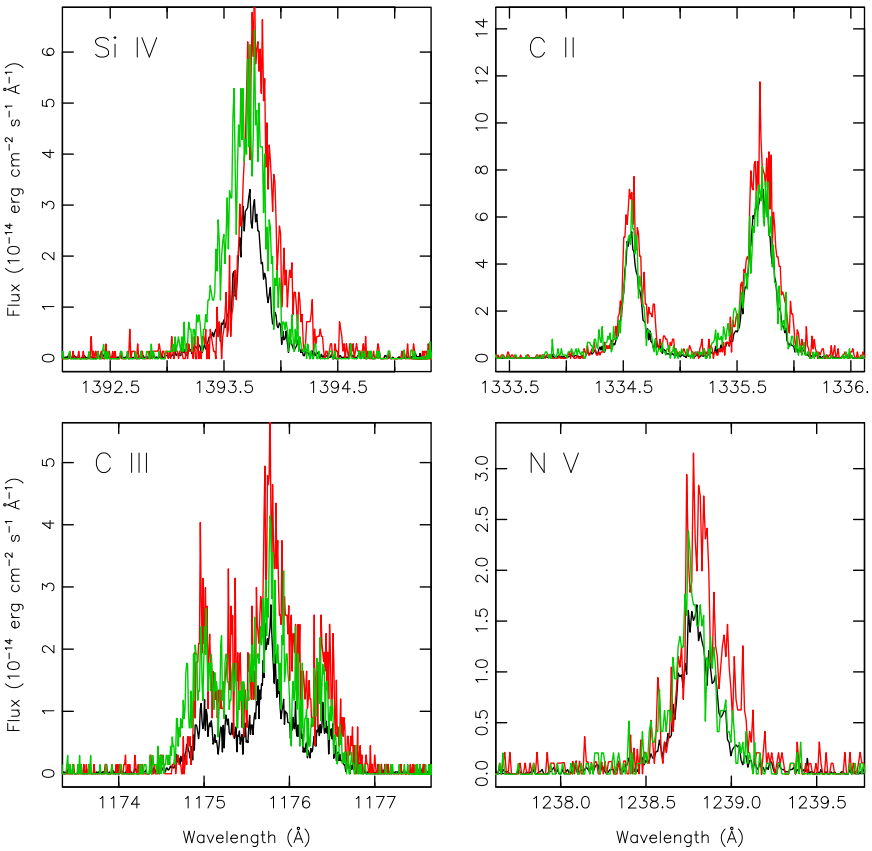


Figure 2. Examples of line profiles in three spectra: average of first orbit (black), exposure number 5 (red), and exposure number 14 (green). The names of the ions are indicated in the panels. The lines show an increase of flux and centroid shifts at these two exposures.

obtained during the five orbits of our observation. In particular, two of the 20 exposures, corresponding to the fifth and 14th ones, were further split into three time intervals of ∼200 s each in order to follow in greater detail the change of line profiles and fluxes as described in the results session. To this purpose, we used the tasks SPLITTAG and CALCOS to split the time-tagged tables of selected photons and accumulate the calibrated spectra relative to each interval.

For the most prominent lines in each spectrum, we have measured fluxes, line FWHMs, and centroids with respect to the rest wavelength of the lines with an R script. The script calculates the flux as the integral of the line counts in a range of ±1 Å around the rest wavelength of the line. For the C II lines at 1334−1335 Å, we used a 0.5 Å window to avoid cross contamination from the nearby line. Given the spectral type of the star, the background is consistent with zero for all of the lines. The centroid is calculated as the intensity-weighted mean over the range of wavelengths. The FWHMs are calculated as the wavelength intervals where the flux is higher than half of the peak of the line.

3. RESULTS

The average spectrum of the five *HST* orbits is presented in Figure 1, right panel. We can distinguish several lines of Si, C, N, and O ions, other than the H I Lyα line, which is the main feature. Also, the individual spectra of the 20 dithered exposures are of excellent quality and allow firm measurements of line fluxes and centroids. Plots of the line doublets of Si IV, N V, C II, and the multiplet of C III at 1175 Å at the different orbits are shown in Figure 2. Most of the results are based on the analysis of the Si IV doublet at 1393.7/1402.5 Å, the N V doublet at 1238.8/1242.8 Å, the Si II line at 1264.7, and the Si III blend at 1206.5. Tables 3–5 list the fluxes, centroids, and FWHMs of the lines measured in each of the 20 exposures acquired in the five orbits. Figures 3 and 5 show the fluxes, line centroids, and FWHMs as a function of the planetary orbital phases. The fluxes of the lines shows two main increases or brightenings during exposures 5 and 14, seen in the Si and C ion lines, as well as in N V. During the rest of the observations, a small variability is detected at the level of 1−2σ, similar to what is observed at the planetary transit phase using archival observations (see Figure 4). We discuss the quiescent spectrum and the two brightenings in the following sections.

3.1. Quiescent Spectrum

Data from the first *HST* orbit were taken during planetary eclipse and should be devoid of any direct planetary contribution. The line fluxes from the first orbit can be assumed to be the basal fluxes from the star alone, given that the planet is obscured by its star. During orbits III and V the line fluxes are similar to the basal flux, suggesting that any component of planetary origin is negligible at these epochs. We have used the archival data of HD 189733, obtained at the planetary transit, with COS and the same grating (four *HST* orbits, exposures of 900 s each), to check the extent of line variability at those epochs. The variability of the line fluxes of Si and C is recognized in the archival spectra at the 2–3σ level (see Figure 4). Overall, during *HST* orbits I, III, and V, the line

Table 3
Centroids, FWHMs, and Fluxes of the Si IV and N V Lines for Each Exposure

Exposure	Wavelength	FWHM	Flux	Error	Wavelength	FWHM	Flux	Error	Wavelength	FWHM	Flux	Error
			(10^{-15} erg				(10^{-15} erg				(10^{-15} erg	
	(Å)	(Å)	cm^{-2} s^{-1})		(Å)	(Å)	cm^{-2} s^{-1})		(Å)	(Å)	cm^{-2} s^{-1})	
	Si IV 1393.7 Å				Si IV 1402.7 Å				Si II 1264.7 Å			
1	1393.74	0.10	7.13	0.76	1402.77	0.19	3.36	0.68	1264.70	0.18	2.10	0.46
2	1393.74	0.25	6.78	0.74	1402.75	0.19	3.41	0.67	1264.78	0.25	2.33	0.46
3	1393.72	0.19	6.42	0.73	1402.73	0.18	3.26	0.66	1264.84	0.40	1.89	0.44
4	1393.71	0.21	6.43	0.73	1402.72	0.13	3.63	0.67	1264.76	0.35	2.18	0.45
5	1393.83	0.23	23.16	0.78	1402.82	0.29	13.05	0.66	1264.77	0.33	3.01	0.35
5a	1393.84	0.26	45.62	2.14	1402.83	0.25	25.11	1.84	1264.75	0.17	3.69	0.97
5b	1393.83	0.17	14.62	1.61	1402.85	0.19	8.10	1.48	1264.76	0.44	2.84	0.94
5c	1393.80	0.21	11.56	1.33	1402.78	0.32	7.13	1.25	1264.79	0.52	2.59	0.79
6	1393.79	0.17	9.16	0.58	1402.77	0.29	4.79	0.51	1264.77	0.42	2.14	0.32
7	1393.75	0.16	7.21	0.55	1402.78	0.08	3.78	0.48	1264.80	0.32	2.10	0.32
8	1393.75	0.20	6.85	0.54	1402.77	0.14	3.83	0.49	1264.81	0.42	2.20	0.32
9	1393.73	0.17	6.40	0.54	1402.76	0.28	3.37	0.48	1264.75	0.39	2.02	0.32
10	1393.73	0.16	6.82	0.54	1402.74	0.06	3.07	0.48	1264.79	0.39	1.84	0.32
11	1393.73	0.16	7.86	0.56	1402.75	0.15	4.06	0.50	1264.78	0.10	2.10	0.32
12	1393.72	0.23	7.10	0.55	1402.74	0.30	3.63	0.49	1264.80	0.20	1.93	0.32
13	1393.74	0.22	6.36	0.53	1402.74	0.24	2.86	0.47	1264.76	0.37	2.23	0.33
14	1393.68	0.31	22.26	0.77	1402.68	0.30	13.45	0.66	1264.75	0.29	2.37	0.33
14a	1393.74	0.26	8.16	1.46	1402.73	0.11	4.36	1.39	1264.79	0.30	2.06	0.91
14b	1393.68	0.26	33.02	1.95	1402.67	0.29	20.76	1.76	1264.68	0.50	2.17	0.92
14c	1393.67	0.43	24.96	1.55	1402.68	0.59	14.91	1.40	1264.76	0.13	2.78	0.78
15	1393.75	0.14	8.13	0.57	1402.73	0.18	4.39	0.50	1264.77	0.35	2.04	0.32
16	1393.73	0.17	6.63	0.54	1402.75	0.16	3.73	0.49	1264.83	0.43	2.26	0.33
17	1393.76	0.12	6.58	0.54	1402.76	0.16	3.63	0.49	1264.75	0.45	2.33	0.33
18	1393.75	0.20	7.43	0.56	1402.73	0.20	3.73	0.49	1264.77	0.12	2.25	0.33
19	1393.75	0.15	6.18	0.53	1402.76	0.05	3.21	0.48	1264.77	0.09	2.00	0.32
20	1393.75	0.19	6.53	0.54	1402.73	0.25	3.21	0.48	1264.81	0.11	2.25	0.33

Table 4
Line Measurements as in Table 3 for Lines of Si III and C II Doublet

Exposure	Wavelength	FWHM	Flux	Error	Wavelength	FWHM	Flux	Error	Wavelength	FWHM	Flux	Error
			(10^{-15} erg				(10^{-15} erg				(10^{-15} erg	
	(Å)	(Å)	cm^{-2} s^{-1})		(Å)	(Å)	cm^{-2} s^{-1})		(Å)	(Å)	cm^{-2} s^{-1})	
	Si III 1206.5 Å				C II 1334.6 Å				C II 1335.7 Å			
1	1206.51	0.18	11.76	0.73	1334.57	0.10	9.45	0.65	1335.70	0.17	17.30	0.81
2	1206.54	0.13	11.31	0.71	1334.58	0.13	8.83	0.63	1335.71	0.21	18.00	0.81
3	1206.54	0.14	10.63	0.70	1334.57	0.09	8.59	0.64	1335.72	0.17	17.64	0.80
4	1206.53	0.19	12.35	0.73	1334.57	0.14	9.17	0.63	1335.70	0.17	17.52	0.80
5	1206.54	0.24	29.16	0.76	1334.60	0.15	15.87	0.60	1335.72	0.21	28.72	0.77
5a	1206.55	0.19	53.50	1.99	1334.61	0.25	21.74	1.44	1335.74	0.18	36.47	1.75
5b	1206.53	0.18	20.12	1.49	1334.59	0.16	13.61	1.26	1335.71	0.25	25.86	1.56
5c	1206.52	0.17	16.43	1.23	1334.59	0.14	12.86	1.08	1335.72	0.20	24.66	1.35
6	1206.54	0.25	14.97	0.59	1334.58	0.11	11.77	0.53	1335.71	0.19	21.99	0.68
7	1206.53	0.13	11.75	0.54	1334.58	0.15	10.39	0.52	1335.71	0.19	20.72	0.66
8	1206.52	0.25	11.74	0.55	1334.57	0.10	10.72	0.51	1335.69	0.20	20.50	0.66
9	1206.50	0.15	11.45	0.54	1334.57	0.10	8.98	0.48	1335.69	0.24	17.90	0.63
10	1206.54	0.14	11.14	0.54	1334.57	0.13	8.81	0.48	1335.71	0.23	18.42	0.64
11	1206.52	0.15	13.55	0.57	1334.56	0.15	9.81	0.52	1335.71	0.18	19.63	0.66
12	1206.54	0.16	12.31	0.55	1334.56	0.15	10.26	0.51	1335.70	0.20	18.54	0.64
13	1206.51	0.20	10.98	0.53	1334.56	0.09	9.19	0.49	1335.70	0.22	17.30	0.62
14	1206.48	0.25	19.60	0.65	1334.55	0.12	12.50	0.55	1335.69	0.22	22.31	0.69
14a	1206.50	0.17	12.22	1.34	1334.57	0.12	10.20	1.16	1335.70	0.23	17.75	1.40
14b	1206.46	0.34	24.29	1.57	1334.55	0.18	13.70	1.27	1335.68	0.13	24.51	1.54
14c	1206.48	0.33	21.79	1.31	1334.55	0.12	13.39	1.08	1335.68	0.21	24.22	1.33
15	1206.53	0.13	12.01	0.55	1334.58	0.11	9.29	0.51	1335.71	0.16	18.59	0.64
16	1206.53	0.12	12.22	0.55	1334.57	0.13	9.89	0.50	1335.69	0.21	17.83	0.63
17	1206.50	0.18	12.49	0.56	1334.56	0.12	9.37	0.49	1335.70	0.24	18.21	0.63
18	1206.52	0.16	12.47	0.56	1334.58	0.12	9.70	0.50	1335.71	0.21	18.44	0.64
19	1206.53	0.18	11.47	0.54	1334.57	0.17	8.83	0.50	1335.71	0.20	18.60	0.64
20	1206.54	0.17	10.56	0.53	1334.56	0.12	9.07	0.49	1335.70	0.22	17.65	0.63

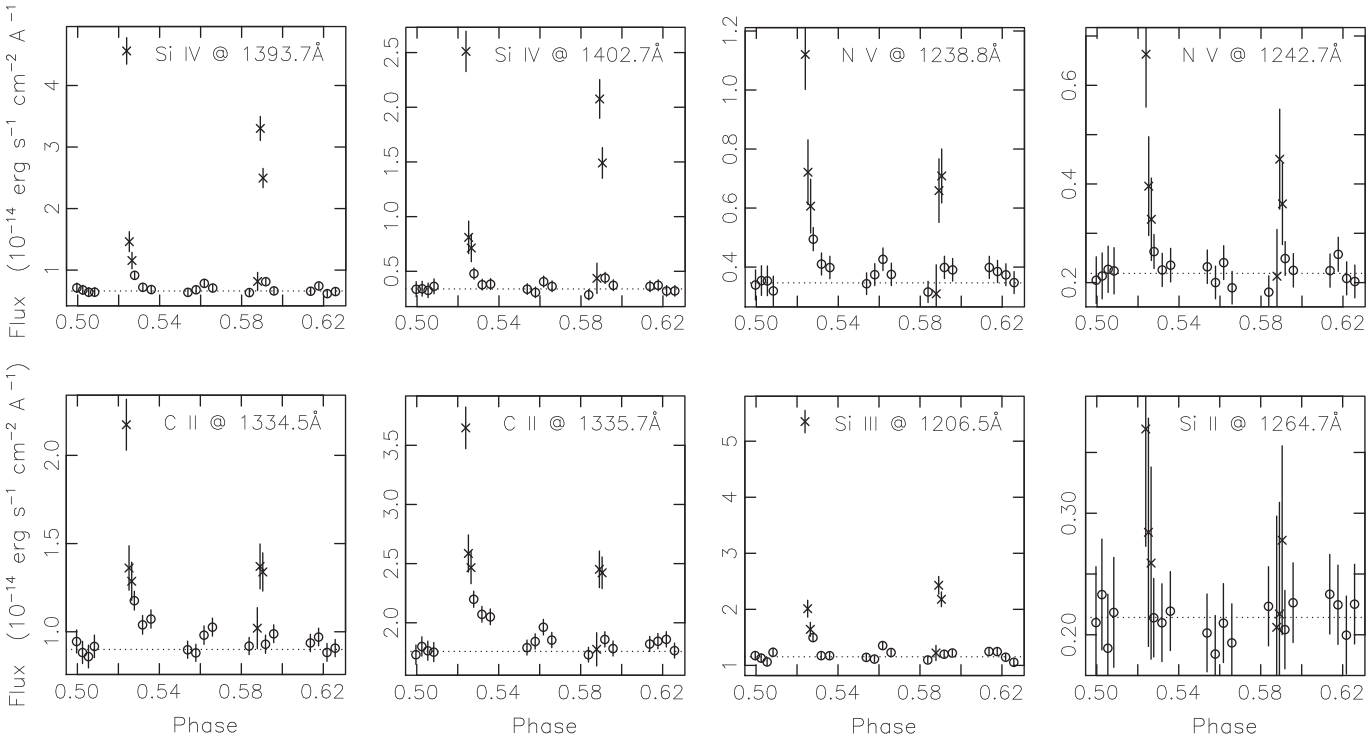


Figure 3. Fluxes of lines as a function of the planetary phases from spectra obtained during our program. The names and the wavelengths of the lines are indicated in each panel. The horizontal line represents the average stellar flux obtained from the first four spectra, i.e., when the planet is completely obscured by the star. Two main episodes of variability are observed at phases 0.525 and 0.588 with duration $t \leqslant 400$ s, for which we obtained subinterval spectra (cross symbols).

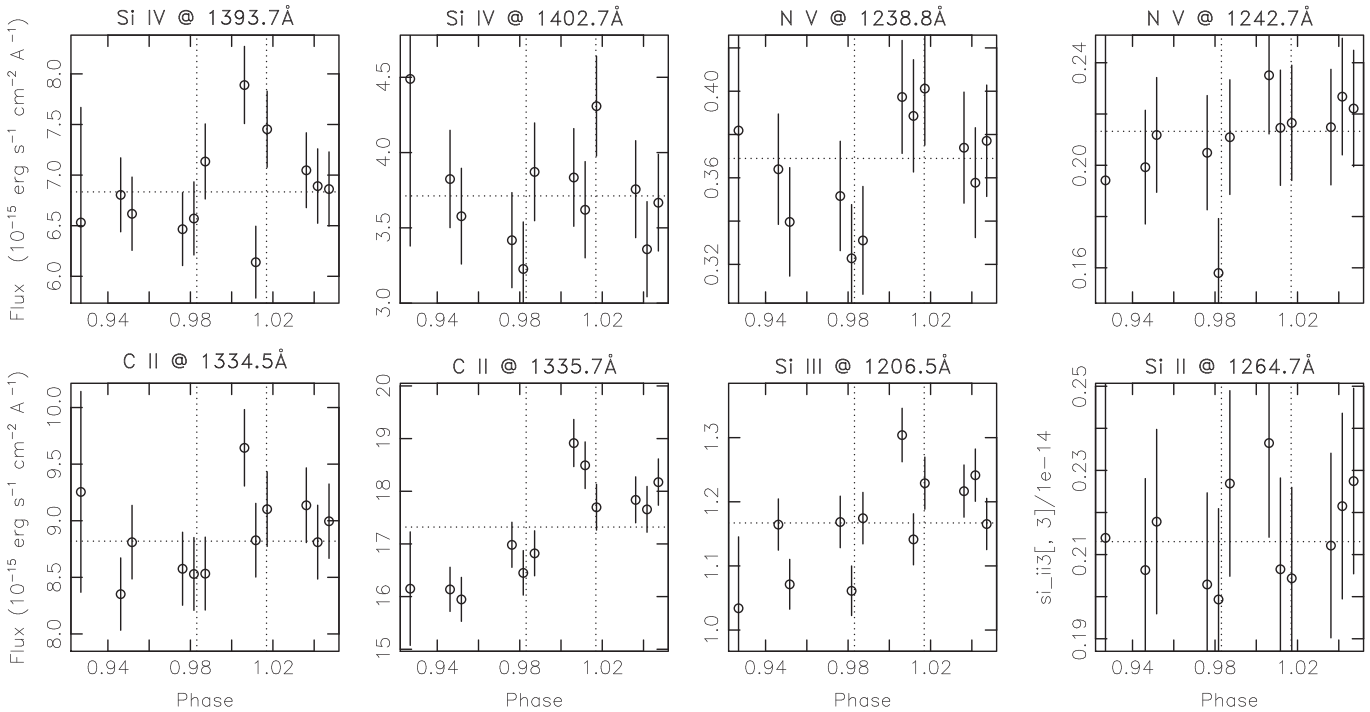


Figure 4. As in Figure 3, fluxes of lines as a function of the planetary phases from archival spectra obtained at the planetary transit. The names of lines are indicated on the top axis. The horizontal line represents the average stellar flux. Variability is observed at the $\leqslant 3\sigma$ level only.

fluxes are consistent to within 1σ, analogous to the transit observations. Moreover, during a planetary transit, the lines of the C II doublet and Si III exhibited a rapid increase and decay at a level of 2σ, markedly visible in the C II line blend at 1335.7 Å. A slow trend superimposed on the rapid increase is also evident in the same C II lines.

The ratio of line intensities gives a diagnostic of plasma temperature, allowing us to determine the basic thermal structure of the emitting plasma and its time evolution. We plot in Figure 6 (top row) the ratios of fluxes as a function of the planetary phase for three Si lines: Si IV 1402.77 Å, Si III 1206.50 Å, and Si II 1264.74. We have assumed as a basal flux

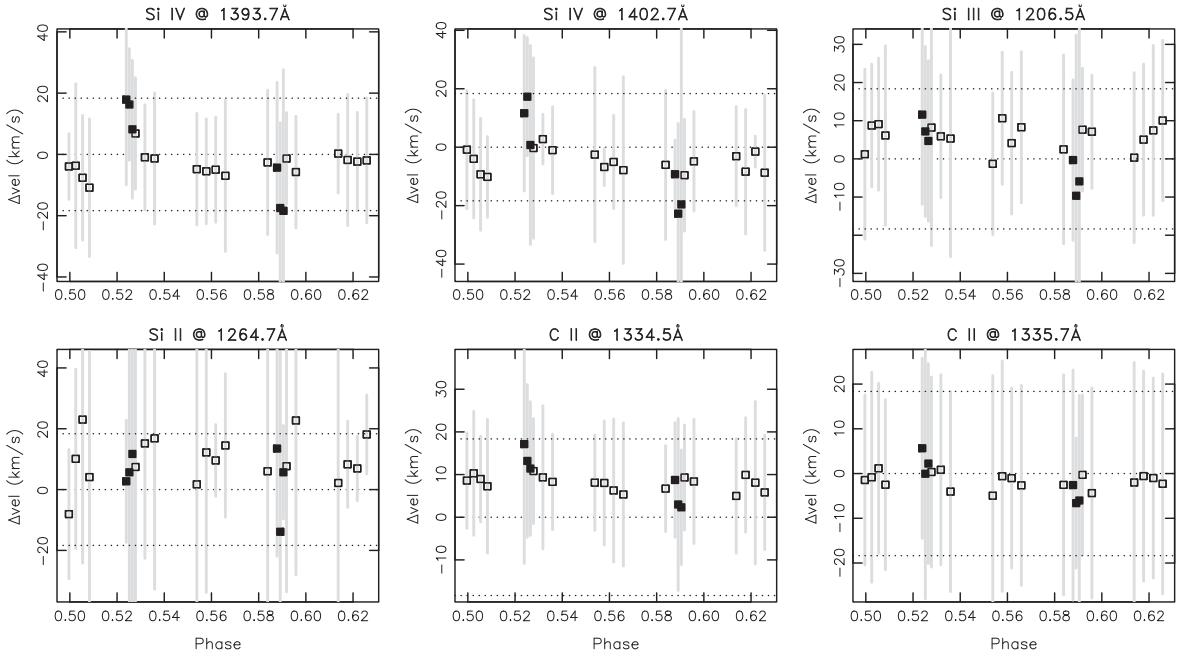


Figure 5. Centroids and FWHMs (vertical segments) of lines as a function of the planetary phases. The horizontal lines mark the values of ± 18.3 km s^{-1}, i.e., the velocity of the subplanetary point at the stellar surface comoving with the planet. For Si ions, the centroid shifts at phases 0.525 and 0.59 are quite close to these values. Filled symbols are the points from subinterval spectra.

the average of the values obtained in orbit I, in exposures 1−4, when the planet is hidden behind the star. For most of the observations (namely, during orbits I, III, and V and part of orbits II and IV), the fluxes and the line ratios show a small scatter within 1–2σ, similar to what is observed at the planetary transit phase. The three ratios Si III/Si IV, Si II/Si IV, and Si II/Si III probe three different temperature regimes. The evolution of the temperature derived from the ratios of Si lines is plotted in Figure 6 (bottom panels). The quiescent plasma has three components, roughly at 80,000, 50,000, and 25,000 K.

The ratios of lines in the doublets of Si IV, N V, and C II are sensitive to opacity effects (Mathioudakis et al. 1999; Bloomfield et al. 2002). In an optically thin plasma, the ratio of the pairs of lines is around two for Si IV and N V and ∼1.8 for C II. Any departure from these values suggests that a dense plasma is present. We have obtained the ratios for the Si IV, N V, and C II doublets for each exposure and compared these with the CHIANTI predictions (Figure 7). We do not observe strong departures from the expected values (the scatter is within 1σ for most of the exposures). On average, the N V ratios show systematically lower values, and the C II ratios show an excess with respect to the theoretical value, whereas the Si IV ratios are in better agreement with the expected value of two. No clear departure is found at the two brightenings. Overall, we conclude that the conditions for an optically thin plasma are met during the exposures, and the small systematic difference in N V and Si IV could be due to uncertainties in the atomic database.

3.2. Line Variability

Two main episodes of flux variability are observed at phases $\phi \sim 0.525$ and $\phi \sim 0.59$, during exposures 5 and 14. We followed the evolution of the spectrum of HD 189733 during these two exposures in more detail, accumulating three spectra from the photons recorded in three shorter time intervals of length ∼200 s, as described in Section 2. In Tables 3–5 we report the measurements obtained in these six time subintervals of ∼200 s each (labeled with 5a, 5b, 5c, and 14a, 14b, 14c, respectively).

The line variability is significant at a level of 8−10σ. The difference in variability at planetary transits and post-eclipse phases is reminiscent of the different X-ray variability observed at transit and posteclipse phases by Pillitteri et al. (2014a, 2011). This suggests the remarkable behavior of the transition region and the corona of HD 189733 after the planetary eclipse and points to a major role for its hot Jupiter.

We discuss in more detail each episode of variability in the next two subsections.

3.3. First Flux Increase

The line profiles of Si and C ions during time intervals 5a, 5b, 5c (top row), and 14a, 14b, 14c (bottom row) are plotted in Figures 13–19. We marked the centroid and the nominal positions of the lines. The figures show in detail the changes of flux, centroid, and widths of these lines on a timescale of ∼200 s.

At the beginning of exposure 5 (second orbit), the line fluxes are already elevated. The interval 5a is the first temporal segment in which we observe HD 189733 when the planet appears in view after its eclipse (see the schematic on Figure 1, left panel, phase range = 0.523−0.527). We were unable to observe the phases between the third and fourth contact, when the planet emerged after the eclipse, so the increase of the line fluxes could have started while the planet was emerging. The line fluxes decrease on a timescale of 400 s, restoring to the basal level for the rest of the *HST* orbit and the subsequent one, until the second flux increase at phase ∼0.59. A small variability is seen during the third *HST* orbit (Figure 3), at a

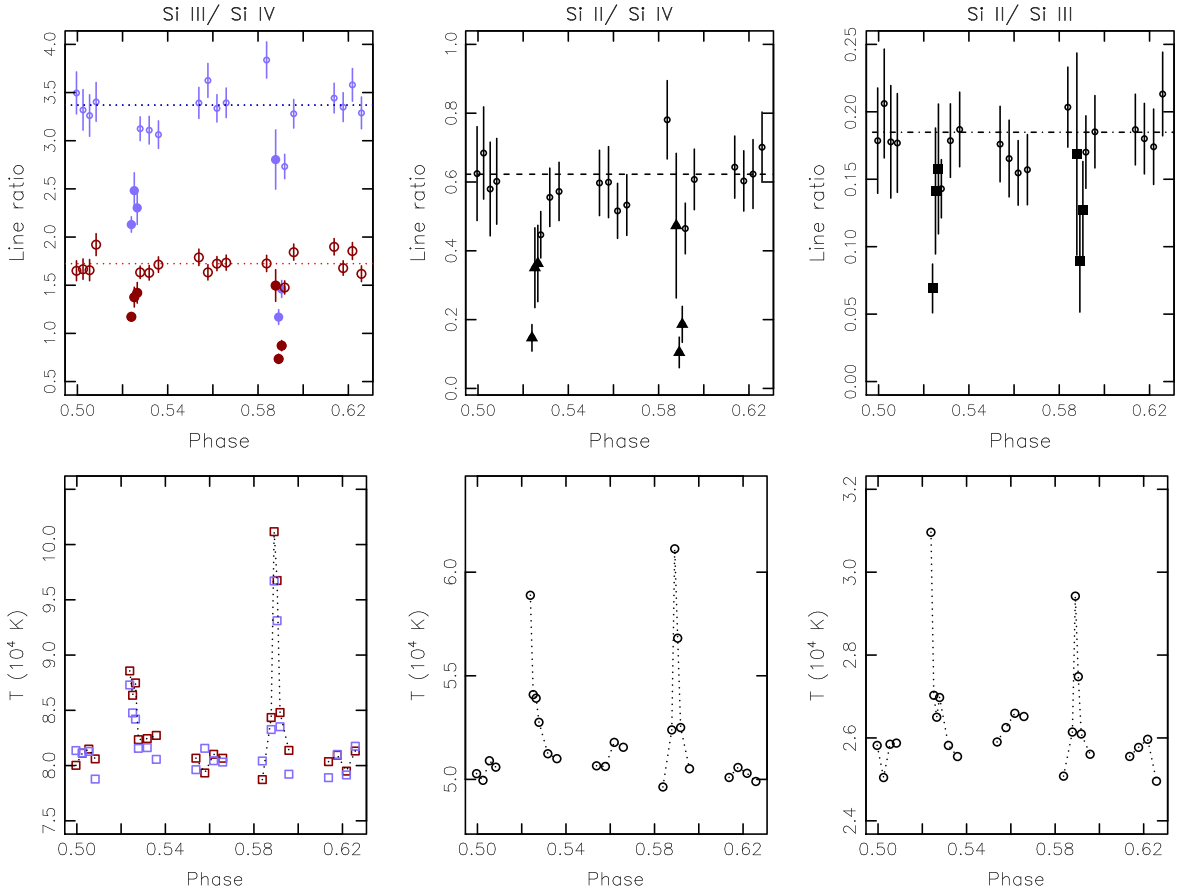


Figure 6. Top row: ratio of Si lines as a function of the planetary orbital phase. Filled symbols are the points from subinterval spectra. Left panel: Si III/Si IV 1402.5 Å (blue symbols), Si III/Si IV 1393.7 Å (red symbols). Central panel: Si II/Si IV 1402.5 Å. Right panel: Si II/Si III. Bottom row: temperature versus planetary phase derived from the line ratios. The comparison of the two peaks shows that the second brightening was hotter in temperature than the first one.

level of 2σ variations and of the same level of variability observed at the planetary transits.

Figure 5 shows the line centroid shifts with respect to the line wavelength at rest (in km s^{-1}) and the FWHMs, as a function of the planetary phases. The uncertainties of the centroids are estimated to be ∼4−5 km s^{-1}. In the same plots, the horizontal lines correspond to the velocity of a point on the stellar surface comoving with the planet orbital period. We also recall that the stellar period is between 11.9 and 16 days (Fares et al. 2010), corresponding to the velocities of 2.5−3.4 km s^{-1} and thus smaller than the speed of the point comoving with the planet (18.3 km s^{-1}).

During the first increase of flux, the centroids of all ions but Si II at the peak of the brightening are shifted redward. For Si IV the pattern is the clearest, with velocity shifts consistent with the comoving planetary speed. For the C II line at 1334.5 Å, the centroid of the line is systematically shifted toward ∼+9 km s^{-1}, and on top of this bias we observe the same pattern of shifts as in the case of the Si IV lines. This systematic redshift is also seen in the archival spectra taken at the planetary transit. A more accurate deblending analysis with IRAF shows that the lines of C II can be fitted with two Voigt profiles, one consistent with the RV shifted stellar wavelength, and the other profile redshifted by ∼20−23 km s^{-1}, which is still consistent with the planetary comoving speed (18.3 km s^{-1}), given the uncertainties of the centroid estimates.

Similar results are obtained when using a cross-correlation technique with the FXCOR task in IRAF. First, we subtracted the spectra of exposures 5a, 5b, 5c and 14a, 14b, and 14c from the average spectrum of the orbit I (after rebinning them by a factor four times the original resolution). For each residual spectrum, a spectral portion around the C II and Si IV doublets was cross-correlated with the average spectrum of orbit I. We find that in exposures 5a, 5b, and 5c the residual spectra are redshifted by up to 20 ± 5 km s^{-1}, whereas in exposures 14a, 14b, and 14c the residual spectra are blueshifted by -20 ± 5 km s^{-1} with respect to the average, basal spectrum of orbit I.

3.4. Second Flux Increase

The second event of variability started at phase ∼0.588 and lasted for about 400 s. It was weaker than the first event. Remarkably, this event along with the X-ray flares observed in 2009, 2011, and 2012 (Pillitteri et al. 2010, 2011, 2014a) occurred in a very restricted range of phases ($\phi \sim 0.52$−0.6). Figure 5 shows that the lines and in particular Si IV and Si III during this brightening exhibit a remarkable blueshift, with Si IV values similar to the planetary comoving speed (∼−18 km s^{-1}). The interpretation of this blueshift is that hot material on the surface of the star, perhaps a hot spot at temperatures of $\sim 10^5$ K, is comoving with the planetary motion and emerging at the stellar limb.

In Figure 8 we plot the empirical cumulative distribution functions (ECDFs) of the time-tagged events that compose three lines of different temperatures of formation, namely C II at 1334.5 Å, Si IV at 1393.7 Å, and N V at 1238.8 Å. Fully

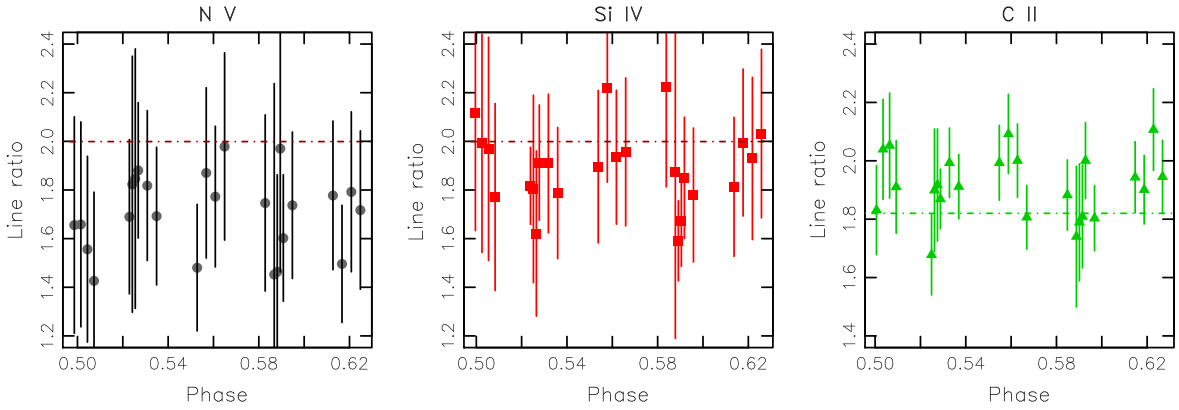


Figure 7. Ratios of lines of doublets of N v, Si iv, and C ii. The horizontal lines mark the expected values in an optically thin plasma. Opacity effects are not detected.

Table 5
Line Measurements as in Table 3 for Lines of C iii Multiplet and N v Doublet

Exposure	Wavelength (Å)	FWHM (Å)	Flux (10^{-15} erg cm^{-2} s^{-1})	Error	Wavelength (Å)	FWHM (Å)	Flux (10^{-15} erg cm^{-2} s^{-1})	Error	Wavelength (Å)	FWHM (Å)	Flux (10^{-15} erg cm^{-2} s^{-1})	Error
	C iii 1175 Å				N v 1238.8 Å				N v 1242.7 Å			
1	1175.71	0.85	10.21	0.96	1238.81	0.19	3.40	0.51	1242.73	0.32	2.05	0.47
2	1175.72	0.74	9.67	0.94	1238.81	0.12	3.54	0.50	1242.75	0.08	2.14	0.46
3	1175.71	0.96	9.17	0.93	1238.81	0.14	3.53	0.50	1242.71	0.16	2.27	0.47
4	1175.72	0.21	10.95	0.96	1238.84	0.18	3.19	0.50	1242.72	0.11	2.24	0.47
5	1175.73	0.96	36.63	1.02	1238.83	0.16	8.03	0.45	1242.76	0.15	4.54	0.39
5a	1175.73	1.56	64.92	2.71	1238.85	0.36	11.20	1.18	1242.76	0.16	6.63	1.07
5b	1175.70	0.22	25.84	2.14	1238.82	0.09	7.21	1.09	1242.79	0.09	3.96	1.00
5c	1175.75	1.03	22.07	1.79	1238.82	0.12	6.06	0.91	1242.72	0.16	3.28	0.83
6	1175.73	0.46	14.92	0.76	1238.80	0.25	4.95	0.39	1242.78	0.18	2.63	0.34
7	1175.73	0.82	12.43	0.73	1238.80	0.24	4.10	0.37	1242.76	0.21	2.26	0.34
8	1175.73	0.18	10.86	0.71	1238.83	0.15	3.99	0.38	1242.73	0.22	2.35	0.34
9	1175.67	0.20	9.39	0.69	1238.82	0.22	3.44	0.36	1242.67	0.19	2.32	0.34
10	1175.74	1.41	10.54	0.71	1238.81	0.23	3.75	0.37	1242.72	0.13	2.00	0.33
11	1175.67	0.33	12.84	0.74	1238.78	0.24	4.27	0.38	1242.80	0.09	2.41	0.34
12	1175.70	1.48	10.33	0.70	1238.82	0.22	3.75	0.38	1242.69	0.98	1.90	0.33
13	1175.68	1.11	9.70	0.69	1238.81	0.19	3.16	0.36	1242.71	0.18	1.81	0.33
14	1175.60	1.39	29.34	0.95	1238.77	0.21	5.70	0.41	1242.76	0.20	3.42	0.36
14a	1175.68	1.45	11.74	1.89	1238.77	0.09	3.09	0.98	1242.78	0.67	2.13	0.95
14b	1175.59	1.27	43.86	2.45	1238.76	0.17	6.59	1.08	1242.74	0.44	4.50	1.01
14c	1175.58	0.27	31.85	1.92	1238.77	0.33	7.09	0.91	1242.76	0.25	3.60	0.82
15	1175.72	0.08	13.33	0.75	1238.80	0.21	3.99	0.38	1242.75	0.28	2.49	0.34
16	1175.69	0.22	10.81	0.71	1238.83	0.14	3.91	0.38	1242.75	0.23	2.25	0.34
17	1175.70	0.12	10.90	0.71	1238.79	0.15	3.99	0.37	1242.76	0.16	2.24	0.34
18	1175.73	0.13	11.03	0.72	1238.80	0.08	3.85	0.37	1242.74	0.12	2.57	0.34
19	1175.70	1.37	10.05	0.70	1238.80	0.19	3.74	0.37	1242.75	0.18	2.09	0.33
20	1175.69	0.11	9.53	0.69	1238.81	0.16	3.48	0.37	1242.75	0.14	2.02	0.33

exploiting the time-tagging feature of COS, these curves allow us to evidence the timing of the line increases. The two sets of distributions are created for events accumulated within 0.5 Å from the nominal line center, during exposures 5 and 14 (*HST* orbits II and IV) that host the two brightenings. During orbit II, the spectral lines start to brighten simultaneously, as demonstrated by the deviation from the purely constant rate (the linear ramp in the dotted line). However, Si iv increases its flux faster than do the N v and C ii lines during the first brightening. The second brightening shows different ECDF shapes: there is a delay between the onset of brightening in N v, Si iv, and C ii, with a peak of N v growth at phase 0.588. The N v line brightening starts earlier and increases at a faster rate than does the Si iv line. Here, the C ii line starts last and is the slowest, nearly exactly the opposite behavior of the first brightening.

The nature of the two brightenings appears to be different: the first is a gradual event, almost simultaneous in the three lines, and less impulsive than the second one. The bulk of plasma temperature in this event is near the peak temperature of the Si iv line, and relatively less plasma is present in the temperature range of the other two lines. The second event is an impulse, with hotter plasma appearing first ($T \geqslant 100{,}000$ K), then in a sequence an intermediate-temperature plasma appears (60,000 K) and, eventually, a plasma as cool as 30,000 K. The nature of this second event is plausible with a flaring episode that is due to an accreting event with a subsequent cooling of the plasma to return to the preflare thermal conditions. The

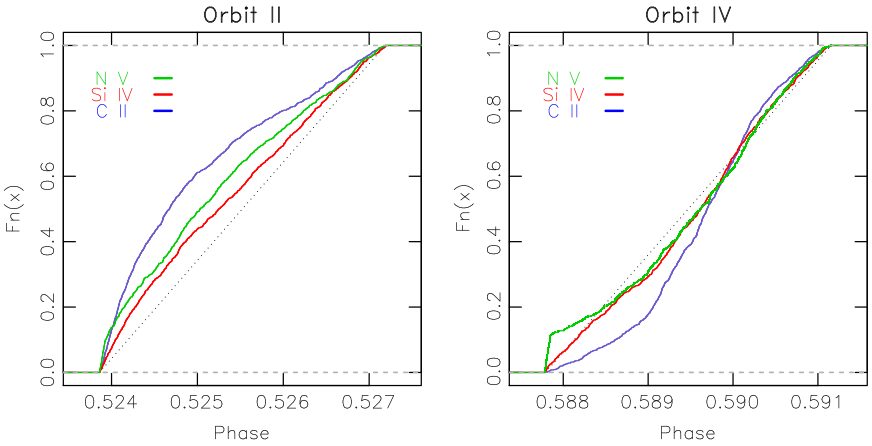


Figure 8. Empirical cumulative distribution functions of events of lines of C II 1334.5 Å (blue), Si IV 1393.7 Å (red), and N V 1238.7 Å (green). The curves refer to the orbits II (left panel) and IV (right panel) during the two line brightenings. A different rise of the lines is observed during the two brightenings, slowly rising in the first one, and hotter, rapid, and impulsive in the second one.

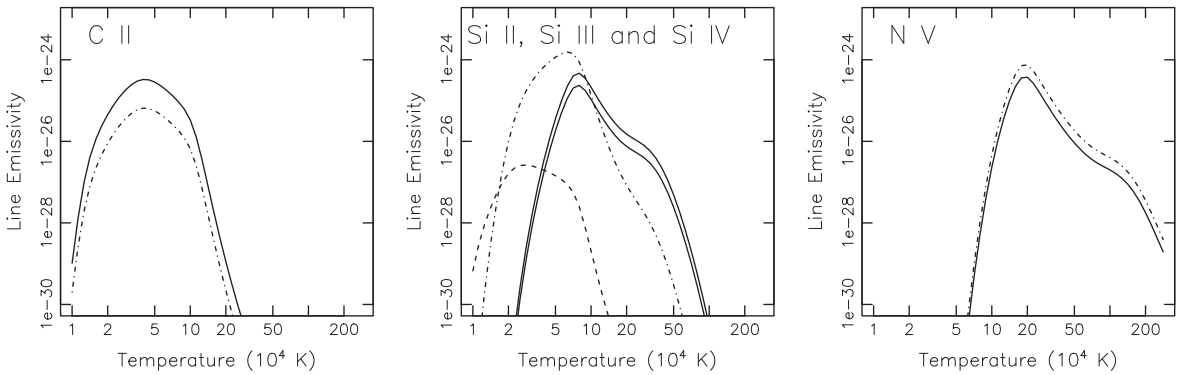


Figure 9. Emissivity of lines in the spectral range 1150−1450 Å. Left: C II doublet. Center: Si II (dashed line), Si III (dot-dashed line), and Si IV doublet (solid line). Right: N V doublet. The curves are derived from the CHIANTI database and *ChiantiPy* routines. The lines are formed in the range $2-50 \times 10^4$ K and thus probe the temperatures typical of the transition region.

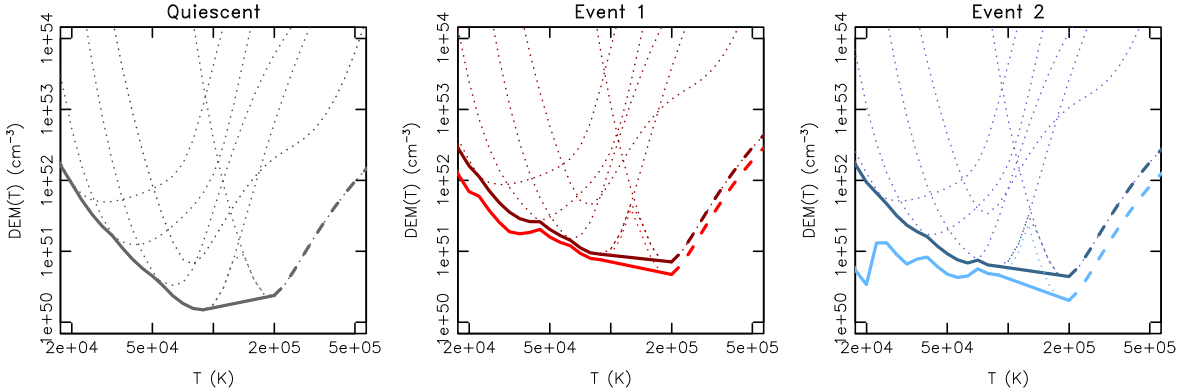


Figure 10. Differential emission measures (DEMs) of the quiescent spectrum (left panel) and the first (central panel) and second brightening (right panel). The dotted curves are the contributions from each line. The DEMs relative to event 1 and 2 are shown as the total DEM (dark-colored curve) and after subtraction of the quiescent DEM (light-colored curve). For doublets of Si IV, N V, and C II we used the sum of the line fluxes and emissivities. Above 2×10^5 K the curves are constrained only by N V.

analysis of the differential emission measure (DEMs) in the next subsection helps to better understand the thermal structure of the plasma during quiescence and the two brightenings.

3.5. Differential Emission Measure

The ion lines in the range of the COS spectra have the peaks of formation temperatures that are typical of the transition region, in the range $T = 10^4-8 \times 10^5$ K (Figure 9). The emissivities are calculated by means of the CHIANTI database and a suite of Python routines, *ChiantiPy 0.5.2* (Dere et al. 1997; Landi et al. 2013). We investigated the thermal structure of the emitting plasma of HD 189733 by means of the DEMs. The DEMs give a measure of the volume and density of a plasma emitting at a certain temperature, and they are calculated by estimating the lower envelope of the contribution

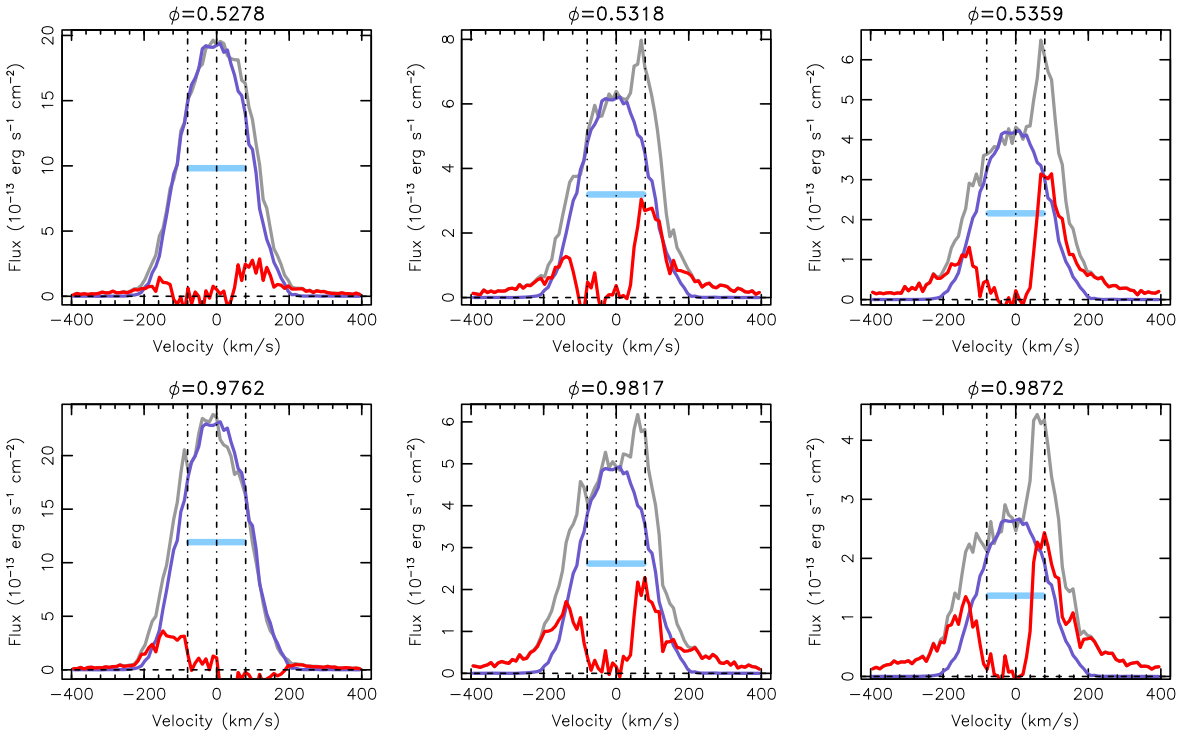


Figure 11. Examples of Lyα profiles corrected for the air-glow emission in Doppler-shift velocity space. The orbital planetary phase is indicated on the top of each panel. The gray line is the raw profile, blue is the air-glow contamination, and red line is the corrected profile. Vertical lines mark the rest position and ± 80 km s^{-1}. The expected width of the uncontaminated and unabsorbed Lyα (150 km s^{-1}) is shown with the light-blue horizontal bar.

of each line (dotted curves in Figure 10). From the emissivity curves and line fluxes, we obtained the DEMs for the quiescent part and the two impulsive events (solid thick lines in Figure 10). The comparison of the values of the quiescent DEM and of the DEMs of the two brightenings and the two slopes around the minimum (occurring at $\sim 8 \times 10^4$ K) shows that during both events more plasma is contributing to the emitted spectrum in the whole range of temperature. For the first event, the emitting plasma is denser or fills a bigger volume than in the quiescent phase. During the second event, the slope of the cool side of the DEM is flatter and steeper than in the quiescent DEM and the DEM of event 1. This means that relatively hotter plasma is present during event 2, and less hot plasma is visible during event 1, indicating again the different nature of the two brightenings, as pointed out before by means of ECDFs. The slope of the DEMs at high temperatures is poorly constrained, being only due to the contribution of the N v doublet, and thus it is identical in all three DEMs.

3.6. Lyα and Other Lines

The main feature in the COS spectra is the H i Lyα line. A detailed analysis of Lyα in the spectra of solar-type stars has been performed by Wood et al. (2005) and, for HD 189733, by Bourrier et al. (2013). Here we attempt a qualitative description of the Lyα as observed with COS; however, a detailed quantitative analysis is beyond the scope of this paper.

The intrinsic Lyα emission of a star of the spectral type of HD 189733 is difficult to assess because of the core absorption due to interstellar gas. Without the narrow geocoronal emission and the strong interstellar medium (ISM) absorption, the line would appear as a double-peaked profile. The ISM absorption almost fully depletes the central part of the profile, and, in addition, deuterium absorption is present at -80 km s^{-1}. The contamination from geocoronal emission has a wavelength width comparable to the COS slit aperture, and it is difficult to subtract (Linsky et al. 2010). Furthermore, the line shows a periodic change in intensity and profile shape as a function of the satellite orbital phase.

We subtracted the air-glow emission from Lyα by using a spectrum obtained during program #11999, which was performed with the same COS setup used in our program. The air-glow spectrum of Lyα has been smoothed with a spline function, corrected for the reflex satellite movement, and resampled on a grid of 0.04 Å centered on the nominal line central wavelength (1215.67 Å) in a range of ± 1.6 Å (394.5709 km s^{-1}). The profiles of our spectra were smoothed and resampled in the same way; the air-glow spectrum was scaled to the median of the five bins around the central wavelength and subtracted from our spectra. The results offer a way to qualitatively discuss the "decontaminated" Lyα of HD 189733 and compare the profile at the planetary transit and planetary eclipse.

We plot in Figure 11 the profiles of Lyα of HD 189733 corrected for air-glow emission, at three epochs, taken after a planetary eclipse and before a transit. We chose these phases as representative of the behavior of the line as a function of the air-glow contamination. When the air-glow emission is at its maximum (left panels in top and bottom rows), the correction suffers more from uncertainties, likely due to the saturation of the line peak in the detector. In the other cases, the correction seems to be more effective, and the double-peaked profile is recovered. In almost all cases, the red peak is higher than the blue peak, as observed sometimes in other stars (see Figure 6 of Wood et al. 2005); this is likely due to the shape of the interstellar absorption being more effective in the blue wing of the line, while the extra deuterium absorption has a narrow

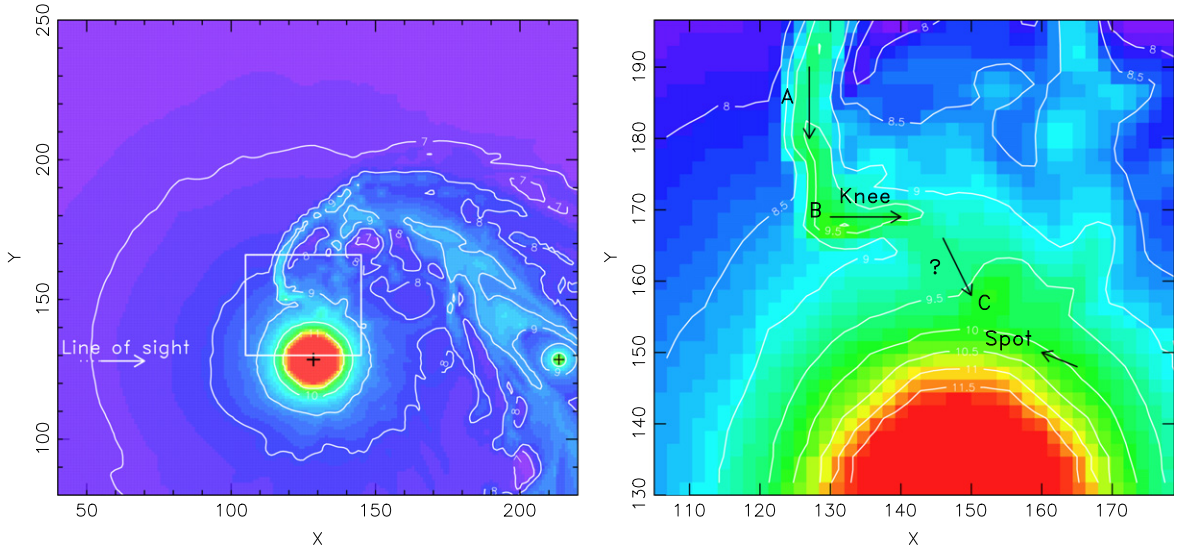


Figure 12. Particle density contours (units of cm^{-3}) of an MHD simulation that models star–planet interactions between a hot Jupiter and its host (polar view). The flow morphology provides a strong candidate scenario to address the FUV line variability of HD 189733 (the observer is viewing the system from the left side). The star rotates counterclockwise, and the planet orbits the star along the same direction. The two "+" symbols shown on the left panel indicate the location of the star (red disk) and the planet (green disk). A close-up of the impact region is depicted in the right panel, where the motion of the accreting plasma is marked with arrows. Specifically, the shocked plasma is funneled by the magnetized stellar wind in an almost radial trajectory close to the star (A), forms a "knee" structure that consists of hot and dense plasma (B), and then accretes in a spot ahead of the orbital phase (C). The precise details of accretion are not investigated by the simulation (zone marked with ?). The knee (B) of the stream and the active spot upon impact on the surface (C) are the main sites of production of the enhanced flux observed in the FUV and X-ray bands and phased with the orbital motion.

effect in the blue portion at around $-80\,km\,s^{-1}$ (Lecavelier Des Etangs et al. 2010; Bourrier et al. 2013).

The average COS spectrum of HD 189733 (with an exposure of 12.106 ks) shows other small lines besides the Si, C, and N ion lines we have analyzed in detail. Lines of Fe XII (1241.8 and 1349.4 Å) and Fe XIX (1328.8 Å) are visible in the spectrum of the total exposure. These lines are from hot material composing the corona of HD 189733. A few very faint unidentified lines are present at 1274.95, 1289.9, 1359.2, and 1360.2 Å.

4. DISCUSSION

We have observed HD 189733 for five consecutive orbits of *HST* during which the planet orbited through the phases $\phi \sim 0.5-0.63$. We obtained time-resolved spectroscopy with COS around Lyα, and we observed two intense line brightenings. A similar strong variability has been observed previously in the same phase range in X-rays (Pillitteri et al. 2010, 2011, 2014a). At these planetary phases, the star systematically manifests an extraordinary, rapid variability in the form of FUV brightenings and X-ray flares. While these events seem typical for an active star, the restricted phase range in which they manifest is anomalous and strongly points to an activity phased with the motion of the hot Jupiter around its host star. HD 189733 is markedly active when the planet is emerging from its eclipse. Supporting this phenomenon is the fact that multiple observations of HD 189733 obtained at the planetary transits both in FUV and X-rays (Lecavelier Des Etangs et al. 2010; Poppenhaeger et al. 2013) did not show similar levels of variability (this being on the order of the $\sim 2-3\sigma$ level), raising the question of why the star is more active when the planet is emerging from its eclipse.

In the following, we propose a scenario where the planet is inducing a relatively compact hot spot on the stellar surface, which benefits from limb brightening at specific posteclipse phases. In particular, we argue that such phased FUV brightenings and X-ray flares could likely be the signature of star–planet interaction in the form of material evaporating from the planet and accreting onto the star, as suggested by recent three-dimensional (3D) MHD simulations by Matsakos et al. (2015; see also Cohen et al. 2011). The numerical model is set up in PLUTO (Mignone et al. 2007, 2012) and includes a magnetized stellar wind, as well as a planetary outflow[5], with the stellar and planetary magnetic fields assumed to be ~2 and ~0.1 G, respectively. The left panel of Figure 12 shows a snapshot of such a simulation (polar view) in order to highlight the flow structure. In this class of systems (see Matsakos et al. 2015 for a classification of star–planet interactions), photoevaporation drives a strong outflow from the surface of the hot Jupiter, which becomes supersonic and collides with the stellar wind. The shocked material is slowed down by the surrounding stellar plasma and is dragged inward by gravity, forming a spiral-shaped trajectory. As a result, the accreting flow impacts the stellar surface at a location that precedes the subplanetary point.

The right panel of Figure 12 shows a close-up of the accretion region. The effects of the stellar wind and gravity funnel the ionized stream through an almost radial trajectory toward the star (point A, right panel of Figure 12). The motion of the infalling material is obstructed by the pressure (thermal plus magnetic) of the stellar corona at a finite height above the stellar surface (point B). At that location, the flow forms a hot and dense structure (the "knee"), with number densities up to[6]

[5] The simulation does not include photoevaporation explicitly. Instead, Matsakos et al. implemented the planetary outflow profile from the detailed simulations, whose results agree with Murray-Clay et al. (2009). See Matsakos et al. (2015) for details of the implementation.

[6] The physical mechanisms necessary to describe accurately the plasma temperature were computationally prohibitive given our numerical resources. Therefore, we do not model the temperature distribution.

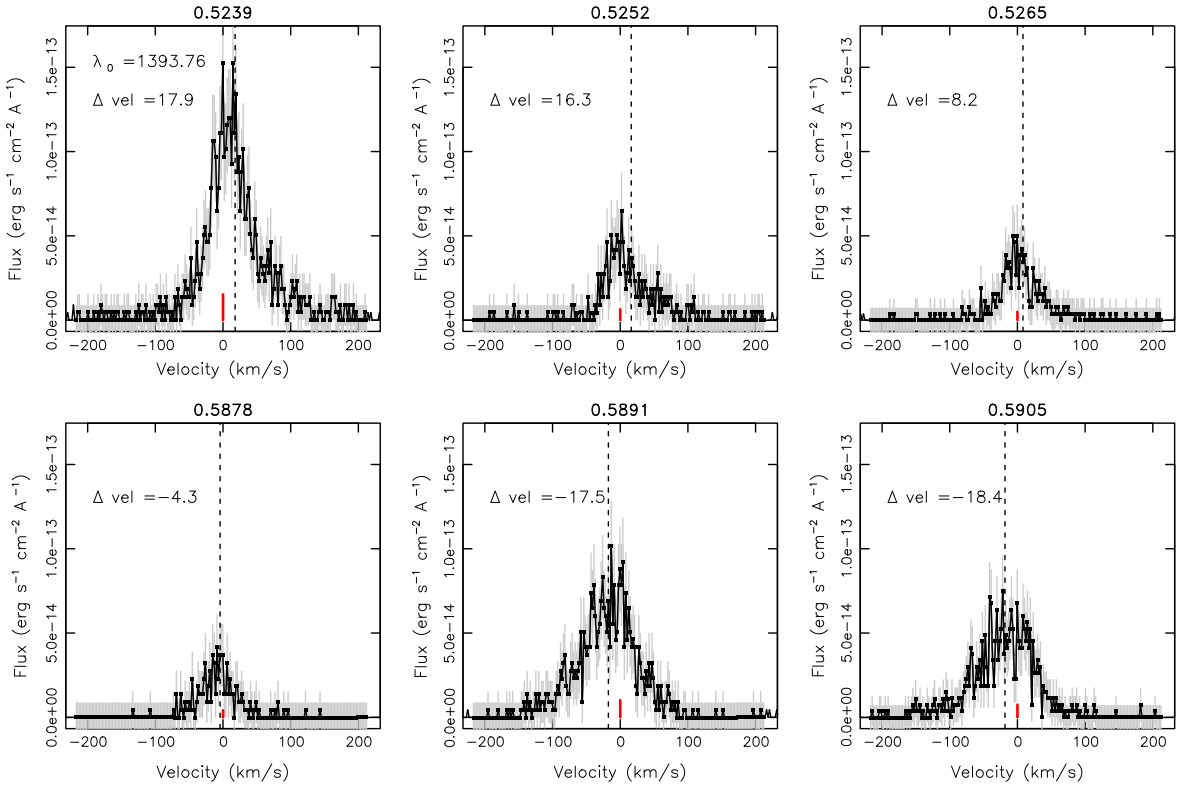


Figure 13. Line profiles of Si IV at 1393.7 Å. We show here the spectra from the three subexposures of ∼200 s of 5a, 5b, 5c, 14a, 14b, and 14c. The values of the planetary phases are indicated on the top axis of each panel. The vertical line marks the centroid of the line, and the red segment is the rest line wavelength (value shown in the top left panel). The differences between centroid and rest wavelength in velocity space (km s^{-1}) are indicated in each panel (corrected for stellar radial velocity, RV = 2.6 km s^{-1}).

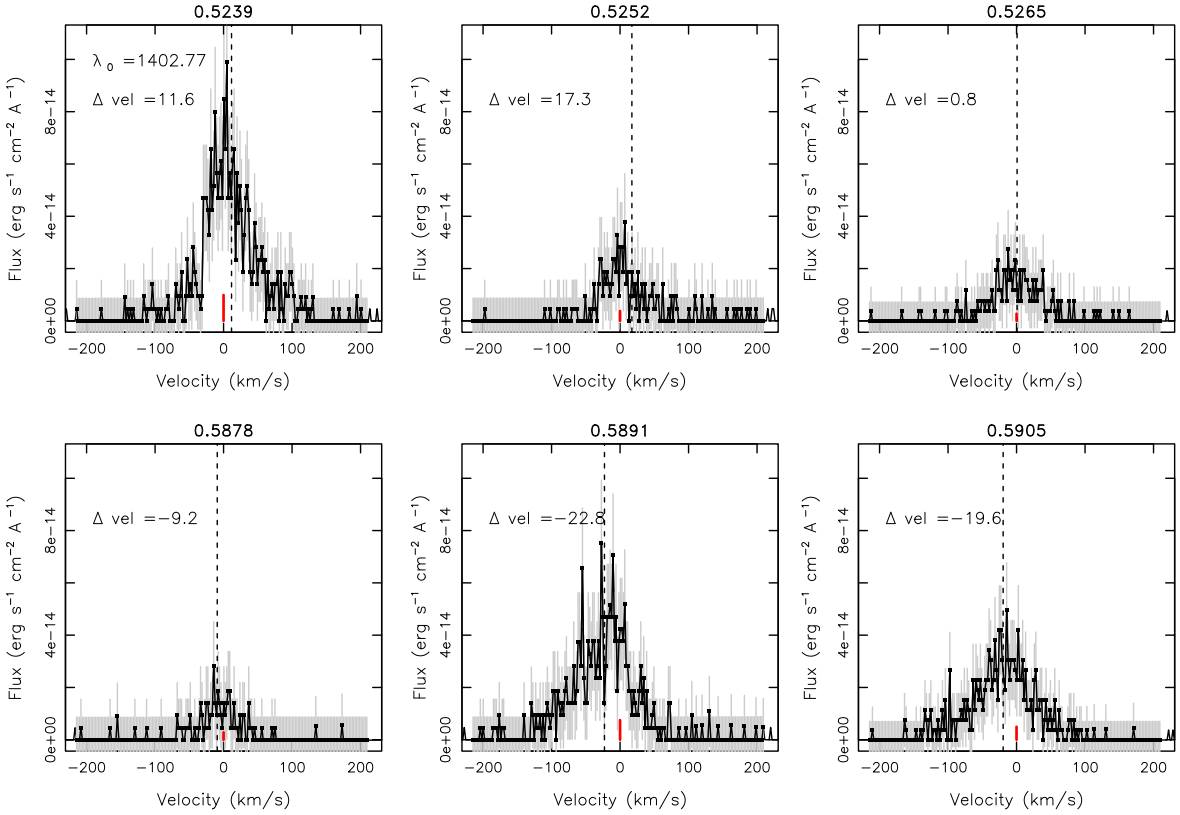


Figure 14. Same as in Figure 13 for the Si IV line at 1402.8 Å.

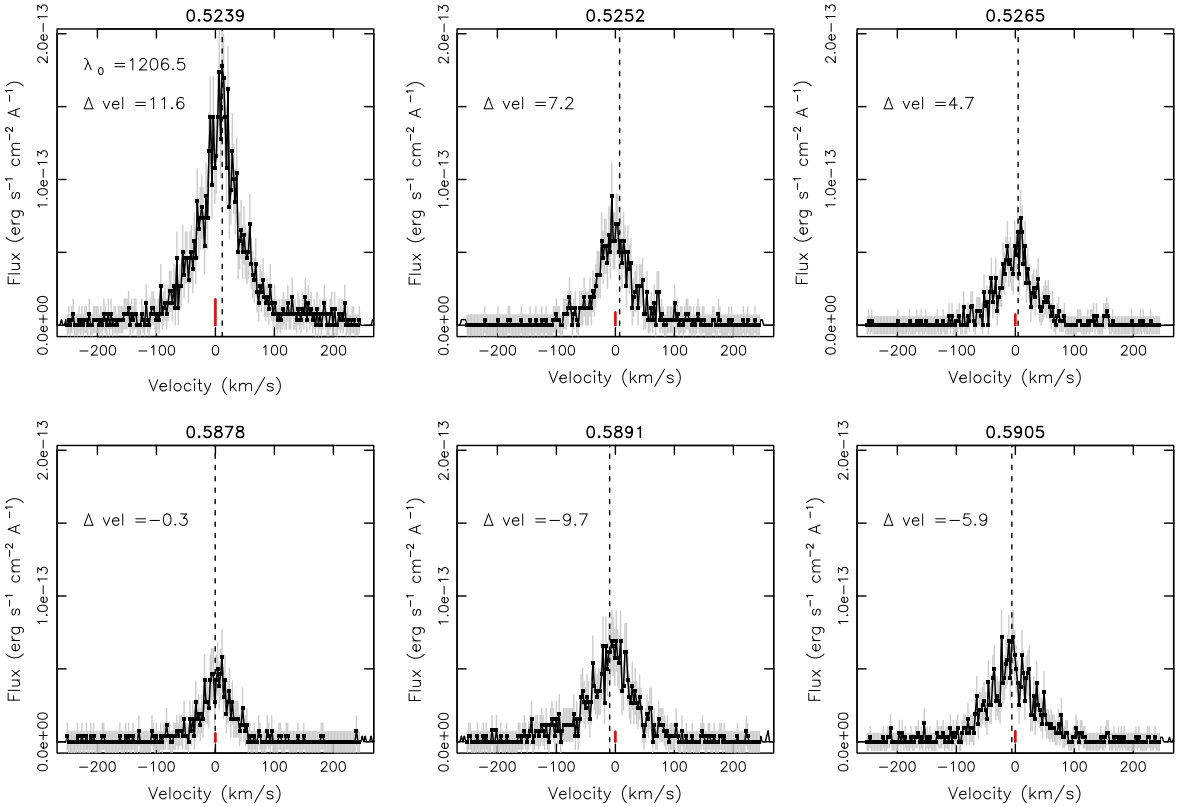


Figure 15. Same as in Figure 13 for the Si III line at 1206.5 Å.

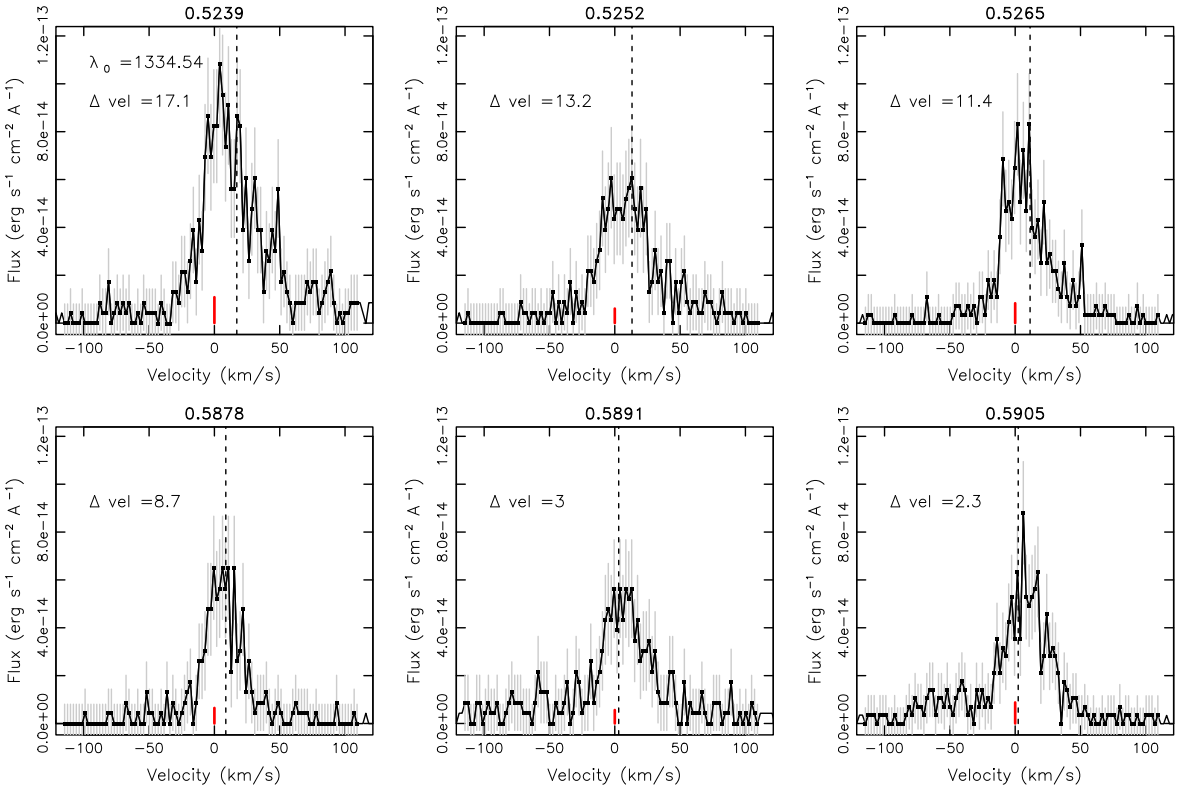


Figure 16. Same as in Figure 13 for the C II line at 1334.5 Å.

10^8 cm^{-3}. Recent planetary outflow models from Koskinen et al. (2013) suggest 6−10 times higher mass loss rates than from Murray-Clay et al. (2009), which would increase the knee density value found in our simulation. In addition, cooling mechanisms could also contribute to condensing the gas. Note that the whole spiral-shaped stream corotates with the hot

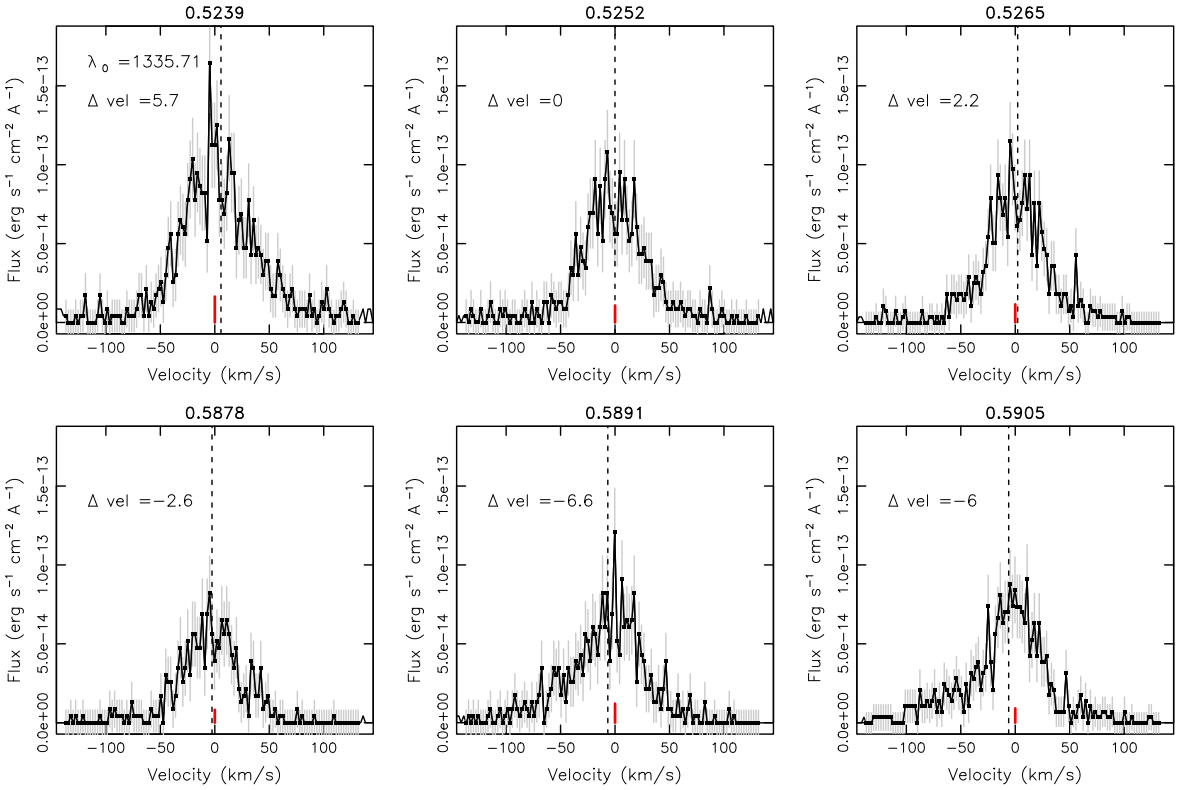


Figure 17. Same as in Figure 13 for the C II line at 1335.7 Å.

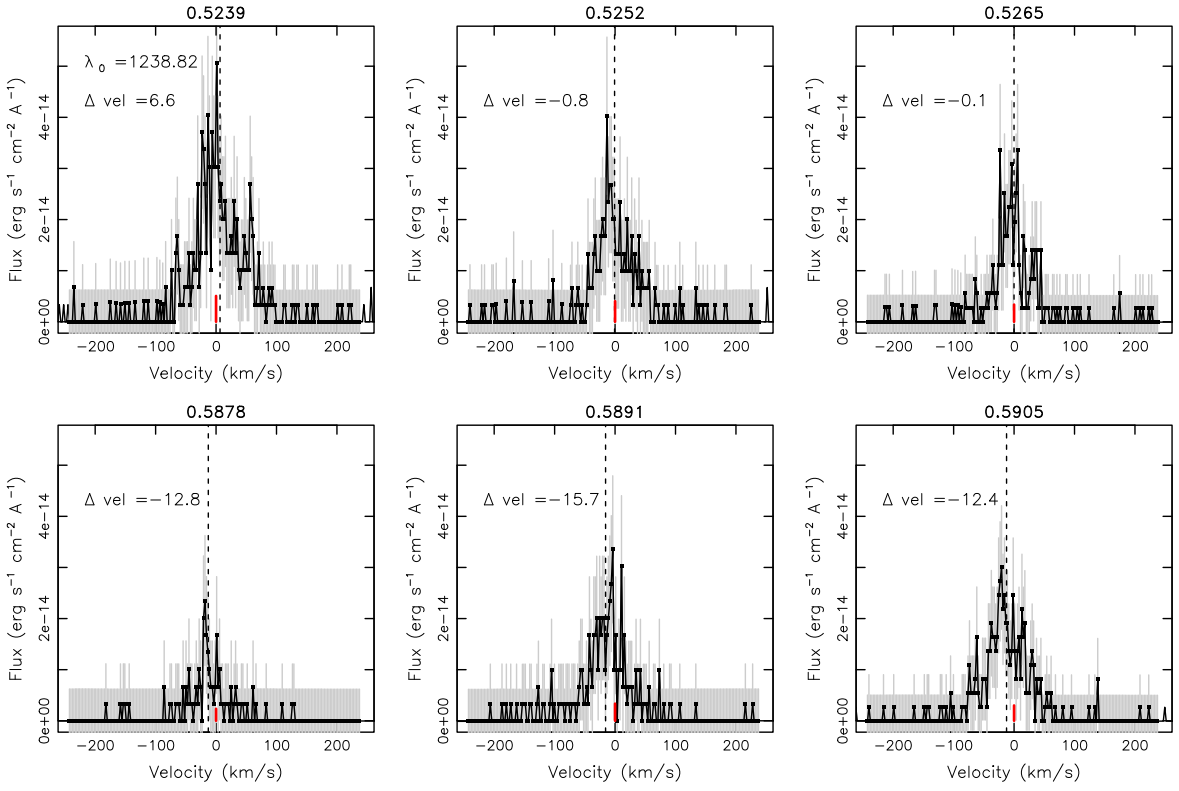


Figure 18. Same as in Figure 13 for the N V line at 1238.8 Å.

Jupiter, and hence, both points A and B rotate around the star with an angular velocity similar to that of the planetary orbit ($P_{\rm pl} \sim 2.2$ days). However, the material that accumulates in point B experiences the drag of the slower rotating star ($P_* = 11.9$ days), and as a result, it loses its angular momentum and lags behind. In addition, the local pressure distribution pushes the gas to the right, leading to the formation of the "knee" structure highlighted in the right panel of

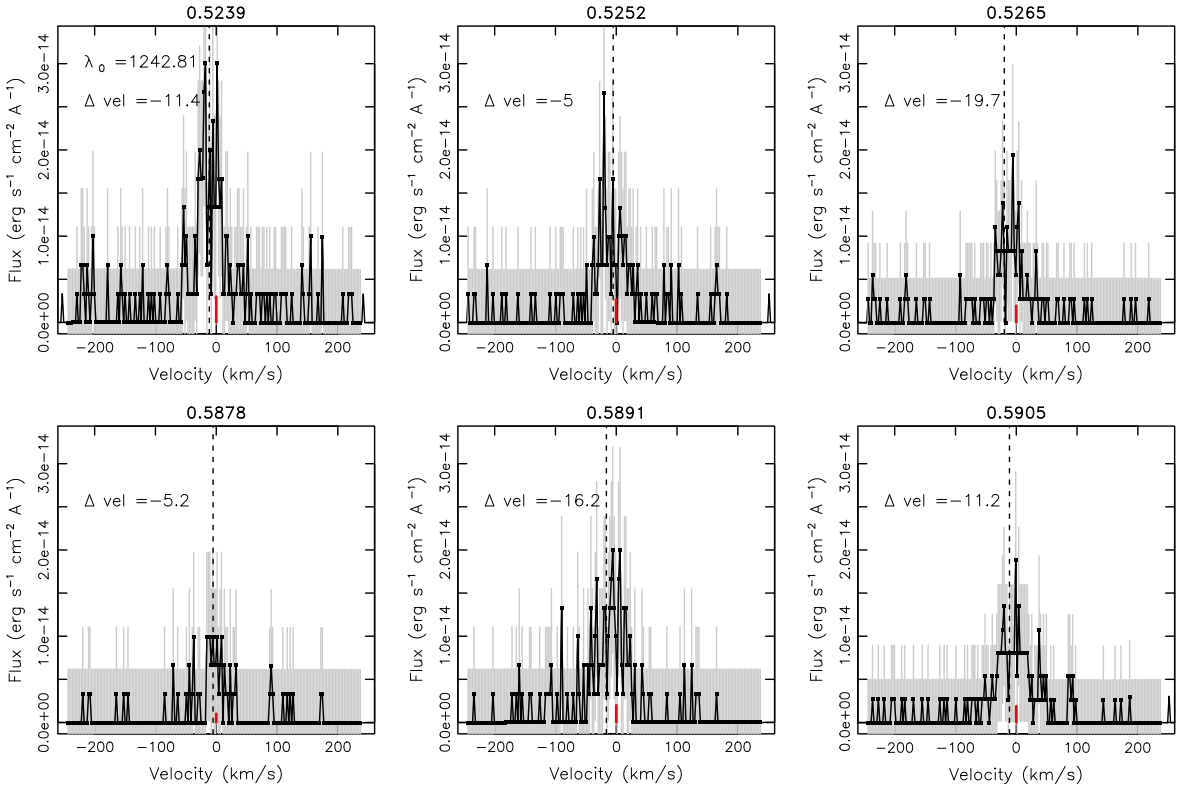


Figure 19. Same as in Figure 13 for the N v line at 1242.8 Å.

Figure 12. The material then accretes onto the star, impacting the chromosphere at point C. A visual inspection suggests that point C precedes the location of the planet by about 70°−90°. As the planet orbits around the star, point C is continuously relocated, effectively corotating with the planet (but the accreted material should acquire the rotation of the star after the impact on the surface). Due to the weaker magnetic fields of main-sequence stars, the accreting plasma is not expected to impact at high latitudes as in protostars.

For the discussion that follows, consider the observer (Earth) to be on the left side of Figure 12 (the line of sight—(LOS)—is depicted with an arrow in the left panel), thus observing the planet after its eclipse. At phase ∼0.52, the elongated structure of hot material in point B is approximately aligned with the LOS. Because the plasma motion is receding with respect to the observer with a velocity of 10–50 km s^{-1}, its emission will appear redshifted. Shortly after, the impact region (point C) appears at the stellar limb along the LOS. The hot spot moves toward the observer with the angular velocity of the planet, corresponding to a local speed of 15–20 km s^{-1} that will blueshift the emitted radiation.

In this context, we find a plausible match between the accretion features in the MHD simulations and the FUV observations. The first brightening can be attributed to the *knee* coming into view approximately when the planet is emerging from the eclipse (point B). The observed redshift is in agreement with the simulation where the flow is receding along the LOS. Because of the shock that is likely to form there, the gas in the knee is expected to be hotter than the average temperature of the transition region, but still cooler than the gas impacting the surface of the star.

The second brightening can be attributed to the spot emerging later at the limb, which is due to the impact of the accreting gas on the chromosphere. It is plausible to imagine that the accreting spot is forced to move with the comoving speed of the planet at the stellar surface (∼18.3 km s^{-1}) because the stream inherits the angular speed of the orbit. As a result, a blueshift of the lines is observed because the spot is moving toward the observer, and at a rate that is faster than the rotational velocity of the stellar surface (3.4 km s^{-1}).

Note that secondary flows may detach from the main body of the stream and fall onto the surface with minor impacts. Nevertheless, the spot of the bulk accretion remains confined in a restricted range of planetary orbital phases and remains within the range of phases in which we observed variability in *XMM-Newton* and in the present *HST* observations.

The accreting stream is moving in an elongated magnetized region (marked by points A and B of Figure 12) that can host magnetic reconnection (and thus flaring activity). The relevant size is markedly different from the typical sizes of coronal loops of main-sequence stars like the Sun. An estimate of the size of such long structures has been inferred from the analysis of the decay light curve of a flare observed in X-rays (Pillitteri et al. 2014a), and it is a few stellar radii. From the simulations, we estimate that the stream forms an arc before the knee of the size of 1.5−2 stellar radii, and the knee is about 1.5 stellar radii above the stellar surface. The mass flux through the knee is estimated to be on the order of a few units of 10^{-8} gr s^{-1} cm^{-2}. From this mass flux, assuming an accreting tube with a section of $0.1 \times R_*$, we estimate a mass accretion from the planet of $\sim 5 \times 10^{18}$ gr yr^{-1}, or up to about 1% of a Jupiter mass in ∼4 Gyr, if the accretion were steady during this period of time.

We warn that the numerical model does not have adequate resolution to model in detail the path of the plasma flowing from point B to C (limited by the demanding nature of 3D MHD simulations). The precise location of the spot (point C)

may vary slightly due to the time dependence of the plasma dynamics. It is plausible that the accretion is not happening in the form of a continuous flow, but instead the plasma accumulates until the density of the gas excedes the confining pressure of the magnetic field and mimicks the fall of dense fragments observed just after the solar eruption of 2011 June 7 (Reale et al. 2013, 2014). The limitations of the numerical simulation prevented us also from following in detail the impact onto the stellar surface. The surface is treated as a boundary that does not physically describe the chromosphere, but rather the base of the stellar wind.

Such MHD simulations of systems harboring hot Jupiters differ from previous simulations (e.g., Cohen et al. 2011) in the treatment of the stellar and planetary winds. They also differ from analytical models of purely magnetic star–planet interaction (Lanza 2009; Lanza et al. 2010, 2011). However, all of these modeling attempts concur to qualitatively describe a preferred planetary phase range in which stellar activity is enhanced by magnetic reconnection or by accreting material, as in the model presented above from Matsakos et al. (2015).

Stars accrete material from their circumstellar disks during the pre-main-sequence phase, and, depending on the rate of accretion, they are identified as classical T Tauri stars (CTTSs, strong accretors) and weak-line T Tauri stars (WTTSs, weak accretors). Given that we make the hypothesis that HD 189733 is accreting material from its hot Jupiter, a comparison between the spectrum of HD 189733 and CTTSs and WTTSs is in order. Ardila et al. (2013) present an extended and thorough analysis of the FUV spectra of a sample of CTTSs and WTTSs. They recognize a broad and a narrow component in the C IV, Si IV, and N V lines, with the relative weight of the narrow to broad component varying between 20 and 80% as a function of the accretion rate. The lines of WTTSs are shaped mainly by a low redshifted, narrow component. The C IV lines are redshifted in both CTTSs and WTTSs, with the redshift being on the order of 10 km s^{-1} in WTTSs. The FUV lines of HD 189733 differ from those of CTTSs and WTTSs. In HD 189733 we observe narrow lines like in WTTSs and a systematic redshift of C II lines that is usually associated with emission from the gas flowing down in the coronal loops.

We find similarities between the spectral features of HD 189733 and the FUV spectrum of the solar eruption of 2011 June 7. The solar event has been analyzed in detail by Reale et al. (2014). This unusual eruption showed the break of a dense filament that ejected dense fragments that eventually fell down on the solar surface. The dynamics of this eruption is the best template for accreting events in pre-main-sequence stars (Reale et al. 2013) and, in our case, for HD 189733. The brightenings of the C IV doublet at 1550 Å were modeled by Reale et al. (2014) by means of a cloud of fragments hitting the top of the chromosphere. Among the results, Reale et al. (2014) explain the broad component of the FUV lines in accreting stars as being due to the accretion taking place simultaneously at different locations on the stellar surface. They also do not find a continuum increase in the reconstructed spectra of the impacting fragments. In solar flares due to magnetic reconnection, a rise of the continuum flux is observed as being due to the heating process and the rise of the free–bound and free–free contributions (Brekke et al. 1996). The lack of continuum flux increase in the brightenings we observed in HD 189733 is analogous to the solar behavior during the impacts of the dense fragments after their eruption. By means of ECDFs we have established in Section 3.4 that the second event has an impulsive nature. The lack of continuum increase during this brightening is analogous to the lack of continuum increase in the solar event described above. This allows us to consider the second brightening in HD 189733 as an accretion event of planetary material similar to the solar event, rather than a flare due to magnetic interaction or reconnection. The first event is instead due to the emergence of a hotter, elongated region (knee) briefly seen through a favorable LOS.

On the wider context of systems with hot Jupiters, the conditions for establishing a steady accreting stream strongly depend on the stellar wind, the intensity and geometry of the stellar magnetic field, the stellar activity (related to the magnetic activity), and the separation of star and planet (which also controls the rate of evaporation of the planetary atmosphere). In this respect, HD 189733 proves to be one of the most favorable systems where this phenomenon can be detected. The presence of a multi-year activity cycle (see, e.g., Fares et al. 2013), associated with a variability of reconnection events (e.g., Llama et al. 2013), implies alternating periods of active accretion and periods of weak or absent accretion. As a consequence, an activity cycle would explain the lack of systematic phased variability when observing stars after a few years and the on/off behavior observed in the case of HD 179949 (Shkolnik et al. 2008).

We find it unlikely that the two events are related to hot material emitting close to the planet. Such material should be ejected from the planet and inherit a velocity of at least 150 km s^{-1}, which is the orbital velocity of the planet. A similar velocity should be involved in magnetic reconnection events close to the planet. At phases 0.52 and 0.59 the components of such velocity along the LOS are $\geqslant -18$ and $\geqslant -80$ km s^{-1}, respectively. In both cases we should see a blueshift when observing after the planetary eclipse. At phase 0.52 we observe a redshift of about +20 km s^{-1}, thus a difference of $\geqslant 40$ km s^{-1} with respect to the expected Doppler shift of emission from gas close to the planet. For the second event at phase 0.59, the expected blueshift is -80 km s^{-1} from material close to the planet. Such a blueshift is not detected in any of the lines.

SPI events should be synced with the synodic period of the star+planet system, which is about 2.7 days. This value is quite close to the orbital period of the planet, so disentangling this effect from other effects purely related to the planetary motion is difficult. In addition, it would require a continuous monitoring of the star for at least three synodic periods, which is a demanding observational effort not realized to date.

5. CONCLUSIONS

In this paper we have presented a time-resolved spectroscopic analysis of the FUV spectrum of HD 189733 acquired with COS on board *HST*, around the Lyα line in the range 1150–1450 Å. We have observed the phases after the planetary eclipse, for a duration of five *HST* orbits. The spectral range comprises several lines of ionized Si, C, N and O, which form in the range of temperature of 20,000–200,000 K, typical of the transition region.

Two rapid line-flux brightenings have been observed in Si, C, and N lines with a duration of 200–400 s. No similar brightenings have been observed in archival observations of HD 189733 taken with the same instrument at a planetary transit. The first event happens when the planet is emerging

after the eclipse (phase ~0.52), the second event later at phase ~0.59. From the line ratios of Si ions, and with a reconstruction of the DEMs, we followed the evolution of the plasma temperature and the rise of temperature during both events. The time evolution of the line fluxes is different and hint at the different nature of the two events: the evolution of the first event has been gradual within 400 s. The second event has been a rapid impulse observed first in the hot lines of N v, and then in the cooler lines of Si iv and C ii. The second event has also been hotter than the first one. For the second event, we find a strong similarity with the impacts of dense fragments during the solar eruption of 2011 June 7. In particular, both events are impulsive and lack a continuum increase, at odds with solar and stellar flares that are due to magnetic reconnection.

With the help of MHD simulations, we argue that the spectroscopic sequence is the signature of gas that evaporates from the planet and accretes onto the star. In particular, the MHD simulations show that material can effectively escape the planetary surface, become supersonic, and collide with the stellar wind. The interaction leads to the formation of an elongated spiral-shaped stream that precedes the planetary motion and a cometary-type tail that trails the orbit. Near the star, the stream is funneled by the surrounding magnetized plasma and infalls almost radially. The flow is then obstructed by the coronal pressure at a finite height above the stellar surface, possibly forming a shock. The dynamical evolution then leads to the formation of a "knee" structure of dense and hot plasma, which is subsequently channeled inward and impacts the stellar surface. As a consequence, the knee region and the surface accretion spot are hotter and denser than the average transition region of the star. Because the entire accreting stream is corotating with the planet, the phased variability occurs when—under favorable alignment with the line of sight—the knee and the accretion spot emerge at the stellar limb. The phase angle between the accretion spot and the subplanetary point matches quite well with the observed phase lag in X-ray and FUV activity.

This scenario is appealing because it can explain both X-ray and FUV observations after the planetary eclipse. These observations provide the spectroscopic signatures of the accreting planetary gas. However, further monitoring at the postplanetary eclipse phases and on a longer time baseline are needed to confirm the systematic occurrence of such spectroscopic signatures and the enhanced activity of HD 189733 at these particular phases.

I.P. is grateful to H. M. Günther for the help and the discussion of the results. I.P. acknowledges financial support from the European Union Seventh Framework Programme (FP7/2007–2013) under grant agreement No. 267251 Astronomy Fellowships in Italy (AstroFIt). T.M. was supported in part by NASA ATP grant NNX13AH56G. The simulation was carried out with resources provided by the University of Chicago Research Computing Center. This work is based on observations made with the NASA/ESA *Hubble Space Telescope*, obtained at the Space Telescope Science Institute, which is operated by the Association of Universities for Research in Astronomy, Inc., under NASA contract NAS 5-26555. These observations are associated with program #12984. Support for program #12984 was provided by NASA through a grant from the Space Telescope Science Institute, which is operated by the Association of Universities for Research in Astronomy, Inc., under NASA contract NAS 5-26555.

Facilities: HST (COS).

REFERENCES

Agol, E., Cowan, N. B., Knutson, H. A., et al. 2010, ApJ, 721, 1861
Ardila, D. R., Herczeg, G. J., Gregory, S. G., et al. 2013, ApJS, 207, 1
Ben-Jaffel, L., & Ballester, G. E. 2013, A&A, 553, A52
Bloomfield, D. S., Mathioudakis, M., Christian, D. J., Keenan, F. P., & Linsky, J. L. 2002, A&A, 390, 219
Bouchyzz, F., Udry, S., Mayor, M., et al. 2005, A&A, 444, L15
Bourrier, V., Lecavelier des Etangs, A., Dupuy, H., et al. 2013, A&A, 551, A63
Bouvier, J. 2008, A&A, 489, L53
Brekke, P., Rottman, G. J., Fontenla, J., & Judge, P. G. 1996, ApJ, 468, 418
Cohen, O., Drake, J. J., Kashyap, V. L., et al. 2009, ApJL, 704, L85
Cohen, O., Drake, J. J., Kashyap, V. L., Sokolov, I. V., & Gombosi, T. I. 2010, ApJL, 723, L64
Cohen, O., Kashyap, V. L., Drake, J. J., et al. 2011, ApJ, 733, 67
Cuntz, M., Saar, S. H., & Musielak, Z. E. 2000, ApJL, 533, L151
Delgado Mena, E., Israelian, G., González Hernández, J. I., et al. 2014, A&A, 562, A92
Dere, K. P., Landi, E., Mason, H. E., Monsignori Fossi, B. C., & Young, P. R. 1997, A&AS, 125, 149
Fares, R., Moutou, C., Donati, J.-F., et al. 2013, MNRAS, 435, 1451
Fares, R., Donati, J.-F., Moutou, C., et al. 2010, MNRAS, 406, 409
Gonzalez, G. 2008, MNRAS, 386, 928
Israelian, G., Santos, N. C., Mayor, M., & Rebolo, R. 2004, A&A, 414, 601
Kopp, A., Schilp, S., & Preusse, S. 2011, ApJ, 729, 116
Koskinen, T. T., Harris, M. J., Yelle, R. V., & Lavvas, P. 2013, Icar, 226, 1678
Kramida, A., Ralchenko, Yu., & Reader, J. 2012, APS Division of Atomic, Molecular and Optical Physics Meeting Abstracts, Vol. 43 (College Park, MD: APS), D1004
Landi, E., Young, P. R., Dere, K. P., del Zanna, G., & Mason, H. E. 2013, ApJ, 763, 86
Lanza, A. F. 2009, A&A, 505, 339
Lanza, A. F. 2012, A&A, 544, A23
Lanza, A. F., Bonomo, A. S., Moutou, C., et al. 2010, A&A, 520, A53
Lanza, A. F., Bonomo, A. S., Pagano, I., et al. 2011, A&A, 525, A14
Lecavelier des Etangs, A., Vidal-Madjar, A., McConnell, J. C., & Hébrard, G. 2004, A&A, 418, L1
Lecavelier Des Etangs, A., Ehrenreich, D., Vidal-Madjar, A., et al. 2010, A&A, 514, A72
Lecavelier des Etangs, A., Bourrier, V., Wheatley, P. J., et al. 2012, A&A, 543, L4
Linsky, J. L., Yang, H., France, K., et al. 2010, ApJ, 717, 1291
Llama, J., Vidotto, A. A., Jardine, M., et al. 2013, MNRAS, 436, 2179
Mathioudakis, M., McKenny, J., Keenan, F. P., Williams, D. R., & Phillips, K. J. H. 1999, A&A, 351, L23
Matsakos, T., Uribe, A., & Königl, A. 2015, A&A, in press (arXiv:1503.03551)
Mignone, A., Bodo, G., Massaglia, S., et al. 2007, ApJS, 170, 228
Mignone, A., Zanni, C., Tzeferacos, P., et al. 2012, ApJS, 198, 7
Murray-Clay, R. A., Chiang, E. I., & Murray, N. 2009, ApJ, 693, 23
Pillitteri, I., Günther, H. M., Wolk, S. J., Kashyap, V. L., & Cohen, O. 2011, ApJL, 741, L18
Pillitteri, I., Wolk, S. J., Cohen, O., et al. 2010, ApJ, 722, 1216
Pillitteri, I., Wolk, S. J., Lopez-Santiago, J., et al. 2014a, ApJ, 785, 145
Pillitteri, I., Wolk, S. J., Sciortino, S., & Antoci, V. 2014b, A&A, 567, A128
Poppenhaeger, K., Schmitt, J. H. M. M., & Wolk, S. J. 2013, arXiv:1306.2311
Poppenhaeger, K., & Wolk, S. J. 2014, A&A, 565, L1
Preusse, S., Kopp, A., Büchner, J., & Motschmann, U. 2006, A&A, 460, 317
Reale, F., Orlando, S., Testa, P., Landi, E., & Schrijver, C. J. 2014, ApJL, 797, L5
Reale, F., Orlando, S., Testa, P., et al. 2013, Sci, 341, 251
Saar, S. H., Cuntz, M., & Shkolnik, E. 2004, in IAU Symp. 219, Stars as Suns: Activity, Evolution and Planets, ed. A. K. Dupree & A. O. Benz (San Francisco, CA: ASP), 355
Schröter, S., Czesla, S., Wolter, U., et al. 2011, A&A, 532, A3
Shkolnik, E., Bohlender, D. A., Walker, G. A. H., & Collier Cameron, A. 2008, ApJ, 676, 628
Shkolnik, E., Walker, G. A. H., & Bohlender, D. A. 2003, ApJ, 597, 1092
Shkolnik, E., Walker, G. A. H., Bohlender, D. A., Gu, P., & Kürster, M. 2005, ApJ, 622, 1075
Triaud, A. H. M. J., Queloz, D., Bouchy, F., et al. 2009, A&A, 506, 377
Vidal-Madjar, A., Lecavelier des Etangs, A., Désert, J.-M., et al. 2003, Natur, 422, 143
Walker, G. A. H., Croll, B., Matthews, J. M., et al. 2008, A&A, 482, 691
Wood, B. E., Redfield, S., Linsky, J. L., Müller, H.-R., & Zank, G. P. 2005, ApJS, 159, 118